NON-SINUSOIDAL BIAS WAVEFORMS FOR ACHIEVING HIGH ETCH SELECTIVITY

BY

ANKUR AGARWAL

B.Tech., Indian Institute of Technology, Bombay, 2003

THESIS

Submitted in partial fulfillment of the requirements
for the degree of Master of Science in Chemical and Biomolecular Engineering
in the Graduate College of the
University of Illinois at Urbana-Champaign, 2005

Urbana, Illinois

ABSTRACT

Ion energy distributions (IEDs) are one of the primary factors governing the etching or deposition characteristics in plasma-aided microelectronics manufacturing processes. Being important parameters, IEDs and angular distributions have been the subject of several experimental and computational investigations in high-density plasmas. The energy provided to the substrate surface upon ion impact can enhance chemical reactions via several mechanisms, demonstrated in simulation and ion beam experiments, with significant implications for profiles of etched features and etch selectivity, as well as film quality in plasma enhanced physical vapor deposition processes (PECVD).

Control of ion energies is typically obtained by varying the amplitude or frequency of a radio frequency (rf) sinusoidal bias voltage applied to the substrate. The resulting IED, though, is generally broad. Controlling the width and shape of the IED can potentially improve etch selectivity by distinguishing between threshold energies of surface processes. Control of the IED was computationally investigated by applying a tailored, non-sinusoidal bias waveform to the substrate of an inductively coupled plasma. The tailored voltage waveform, a quasi-dc negative bias having a short positive pulse each cycle, produced a narrow IED whose width was controllable based on the length of the positive spike and frequency. Selectivity between etching Si and SiO_2 in fluorocarbon plasmas could be controlled by adjusting the width and energy of the IED. Control of the energy of a narrow IED enables etching recipes that transition between speed and selectivity without change of gas mixture.

ACKNOWLEDGMENTS

I would like to express my profound gratitude to my adviser, Prof. Mark J. Kushner, for his constant support, encouragement and valuable suggestions.

I would like to acknowledge the support of Semiconductor Research Corporation (SRC) and Varian Semiconductor Equipment Associates (VSEA). I am also thankful to Dr. Rajesh Dorai for his constant motivational support and for insightful discussions.

I am also thankful to my fellow members in the Computational Optical and Discharge Physics Group: Arvind Sankaran, Kapil Rajaraman, Vivek Vyas, Ananth Bhoj, Shane Stafford, Ramesh Arakoni, Kelly Collier and Dr. Natalia Y. Babaeva. Thanks also are due to my roommates and friends for making my stay in Urbana-Champaign and in Ames such an enjoyable experience.

I am most indebted to my parents and relatives for their constant support and encouragement throughout the course of my education.

TABLE OF CONTENTS

1. INTRODUCTION

1.1 Development of Plasma Processing Tools

Plasma processing is an important technology for an increasing number of industries, including semiconductor manufacturing, medical products, and environmental pollution control.[1] In particular, low pressure, high plasma density discharges are gaining importance for advanced semiconductor processing in the fabrication of fine features in microelectronics. The trend to shrink modern microelectronic devices is pushing processing technologies to unprecedented limits. Modern processing techniques should therefore meet both the demands of large scale and small scale. To meet the stringent requirements, novel methods of plasma operation are investigated. The demand for plasma etching processes with better uniformity, anisotropy and selectivity has led to the development of high plasma density sources such as inductively coupled plasmas (ICP) and electron cyclotron resonance (ECR) plasmas.

1.2 Tailored Bias Voltage Waveforms: High Etch Selectivity

The primary advantage of plasma assisted etching of materials over wet etching for microelectronics fabrication, is directional etching of small features due to energetic ion bombardment of the substrate.[2] The primary disadvantage is the difficulty of achieving selectivity in etching between two materials due to the dominance of physical as opposed to chemical processes.[3] Highly selective etching is important with respect to preventing excessive erosion of photoresist or underlying materials, and so allows over-etching to compensate for nonuniformities of fluxes across the wafer.[4]

The primary factors that influence etching or deposition profiles include the flux, and energy and angular distributions of reactant species onto the surface of the wafer. The magnitude of fluxes to the wafer are best controlled by varying gas pressure, power deposition, and feed gas mixture. For example, etching of silicon and silicon dioxide in high plasma-density process tools has shown higher selectivity of SiO_2 over Si for feed gases with high carbon to fluorine atom ratios, such as C_2F_6 and C_4F_8, [5,6] or by the addition of H_2.[7,8] In selected cases, etch rates of SiO_2 have been shown to saturate on increasing power deposition in inductively coupled plasmas, presumably due to changes in the composition of the reactants.[9] In this regard, changes in the composition of the ion flux have been shown to not be the major influence on Si and SiO_2 etch rates.[10]

In fluorocarbon gas mixtures, the selectivity of SiO_2 over Si is based on the deposition of fluorocarbon films which regulate delivery of activation energy by ion bombardment to the substrate. Silicon surfaces, which are unreactive with the overlying CF_x polymer, typically support thicker polymer layers which then reduce the delivery of activation energy to the Si surface. SiO_2 surfaces, which react with the polymer, typically support thinner films which allow more efficient delivery of activation energy to the SiO_2 polymer interface. As such, etching of Si generally requires higher ion energies and biases in fluorocarbon plasmas to penetrate the thicker polymer layer than when etching SiO_2.

Selectivity can, in principle, be obtained by directly controlling the energy of ions which bombard the wafer surface. For example, if most ions bombarding the substrate have energies greater than the threshold energy of SiO_2 while being less than that of other materials such as Si, then, in principle, high selectivity can be obtained.[11] The differences in these threshold energies is typically only a few tens of eV, thereby requiring narrow ion energy distributions to obtain

high selectivity. Secondary considerations in controlling the ion energies include the ion angular distribution to prevent aspect ratio dependent etch rates when the depth of the feature increases.[12]

Conventionally, control of the ion energy distribution (IED) at the substrate is obtained by varying the amplitude or frequency of a sinusoidal bias voltage waveform applied to the substrate. For a given voltage amplitude and mass of the ion, the width in energy of the IED can be controlled by varying the bias frequency[13] but this method suffers from two limitations. First, for a given frequency the width of the IED depends on the mass of the ion, being broader for the lighter ions and so maintaining a specified width of the IED is difficult with chemistries having a large variety of ions. Even for high bias frequencies (>10s MHz) the IED tends to be wide for low mass ions in high plasma density reactors which have thin sheaths and short crossing times across the sheath. Second, at sufficiently high frequencies where IEDs for all ion masses are commensurate (>100s MHz), the rf wavelength may become comparable to the substrate dimensions. These nonuniformities in bias voltage across the substrate may produce unacceptable process nonuniformities.[14]

In the thin sheath limit, the energies and angular spread of ions at the wafer primarily depend on the instantaneous voltage drop when the ion enters the sheath. With a sinusoidal bias, the sheath voltage oscillates in time and so a broad IED results. This broad IED may include ions having high enough energy to breach the threshold energies for many materials, and so may not discriminate in etching those materials. Wang and Wendt[15] demonstrated that by using a tailored, non-sinusoidal bias voltage waveform, a narrow IED at the substrate can be achieved. This control is obtained by using a waveform which maintains the sheath voltage at a constant value for the majority of the rf cycle. Ions entering the sheath during this portion of the cycle strike the substrate with nearly a constant energy. Although there are issues associated with

passing high frequency components through a finite impedance of the substrate and chuck, bias waveforms can be constructed to produce the desired sheath voltages.[15] Rauf computationally showed that the sheath voltage above the wafer can be manipulated by the shape of the applied waveform.[16]

1.4 Conclusions

The need to achieve high etch selectivity is clear and the use of tailored bias voltage waveforms is one method to address that need. Tailored bias voltage waveforms can be leveraged in devising etching recipes where the control over etch characteristics will be over the physical component as opposed to the chemical component.

The algorithms developed in this work were incorporated into the 2-dimensional (2d) Hybrid Plasma Equipment Model (HPEM) which is discussed in detail in Chapter 2. As an introduction, the HPEM consists of three modules: the Electromagnetics Module (EMM), Electron Energy Transport Module (EETM), and Fluid Kinetics Module (FKM). The modules are executed iteratively until convergence. The rates and the source functions of electron impact reactions are calculated in the EETM module using Monte Carlo techniques. Investigation of the surface profile evolution for the etch profiles have been done using the 2-dimensional (2d) Monte Carlo Feature Profile Model (MCFPM) which is discussed in detail in Chapter 3.

These models were then used to computationally investigate plasmas sustained in Ar/C_4F_8 gas mixtures in an ICP reactor to study etch selectivity in fluorocarbon plasmas and the results of the simulations are presented in Chapter 4. The concept of etching recipes has been explored and the results have been quantitatively analyzed as a function of peak-to-peak voltage, and time of change of voltage. Finally, conclusions are presented in Chapter 5.

1.5 References

[1] J. R. Roth., Industrial Plasma Engineering, Volume 1. (1995)

[2] M. Armacost, P.D. Hoh, R. Wise, W. Yan, J.J. Brown, J.H. Keller, G.A. Kaplita, S.D. Halle, K.P. Mller, M.D. Naeem, S. Srinivasan, H.Y. Ng, M.Gutsche, A. Gutmann, B. Spuler, IBM J. Res. Develop. **43**, 39 (1999)

[3] E. Collard, C. Lejuene, J.P. Grandchamp, J.P. Gillers and P. Scheiblin, Thin Solid Films **193**, 100 (1990)

[4] M.F. Dowmling, N.R. Rueger, G.S. Oehrlein and J.M. Cook, J. Vac. Sci. Technol. B **16**, 1998 (1998)

[5] T. Fukasawa, A. Nakamura, H. Shindo and Y. Horiike, Jpn. J. Appl. Phys. **33**, 2139 (1994)

[6] J.A. O'Neil and J. Singh, J. Appl. Phys. **77**, 497 (1995)

[7] H.-H. Doh, J.-H. Jim, K.-W. Whang and S.-H. Lee, J. Vac. Sci. Technol. A **14**, 1088 (1995)

[8] M. Haverlag, G.M.W. Kroesen, C.J.H. de Zeeuw, Y. Creyghton, T.JH.J. Bisschops and F.J. de Hood, J. Vac. Sci. Technol. B **7**, 529 (1989)

[9] G.S. Oehrlein, Y. Zhang, D. Vender and O. Joubert, J. Vac. Sci. Technol. A **12**, 333 (1994)

[10] K.H.R. Kirmse, A.E. Wendt, G.S. Oehrlein and Y. Zhang, J. Vac. Sci. Technol. A **12**, 1287 (1994)

[11] S.-B. Wang and A.E. Wendt, J. Appl. Phys. **88**, 643 (2000)

[12] O. Joubert, G.S. Oehrlein and Y. Zhang, J. Vac. Sci. Technol. A **12**, 658 (1994)

[13] W.M. Holber and J. Forster, J. Vac. Sci. Technol. A **8**, 3720 (1990)

[14] J.E. Stevens, M.J. Sowa and J.L. Cecchi, J. Vac. Sci. Technol. A **14**, 129 (1996)

[15] S.-B. Wang and A.E. Wendt, J. Vac. Sci. Technol. A **19**, 2425 (2001)

[16] S. Rauf, J. Appl. Phys. **87**, 7647 (2000)

2. DESCRIPTION OF THE MODEL

2.1. Introduction

In this chapter, the models and the techniques used for these investigations are described. All the algorithms developed in this work have been integrated into the Hybrid Plasma Equipment Model (HPEM). An overview of the HPEM is given here so that the thesis work can be understood in the context of the entire hierarchy.

2.2 Hybrid Plasma Equipment Model (HPEM)

The HPEM is a plasma equipment model developed by the Computational Optical and Discharge Physics Group to numerically investigate low-pressure and low temperature plasma processing reactors in two and three dimensions [1-8]. The HPEM can model a variety of reactor geometries, and it can analyze different gas chemistries and generate the corresponding plasma parameters. A flow diagram of the HPEM is shown in Fig. 2.1. The HPEM addresses the plasma physics and plasma chemistry in a modular fashion. The main modules are the Electromagnetics Module (EMM), Electron Energy Transport Module (EETM), and Fluid Kinetics Module (FKM). The HPEM iterates on these different coupled modules to generate the plasma parameters.

The inductively coupled electromagnetic fields and magnetostatic fields are computed in the EMM, which is discussed in Section 2.3. These fields are used in the EETM to produce electron transport coefficients. Electron Temperature and electron impact rate coefficients as a function of position are obtained by either using an Electron Monte Carlo simulation (EMCS) or by solution of the fluid electron energy equation coupled with a solution of the Boltzmann

equation. The EMCS is also used for electron beam transport. This module is discussed in Section 2.4. Results of the EETM are transferred to the FKM to determine plasma source and sink terms. The FKM solves the fluid continuity equations for species densities and plasma conductivity and solves Poisson's equation for the electrostatic fields. The densities, conductivity, and electric fields obtained from the FKM are then transferred to the EMM and EETM. These three modules are solved successively in a time slicing manner or until a converged solution.

Several in-line modules of the HPEM have been developed for other specific purposes. The Plasma Chemistry Monte Carlo Module (PCMCM) computes energy and angular dependencies of fluxes at specified surface locations by using outputs of the FKM.[9] The Monte Carlo Feature Profile Model (MCFPM) is an off-line module which uses the result of the PCMCM to simulate micro-scale feature profile.[10] The structure of MCFPM will be discussed in Chapter 3.

2.2.1 The Electromagnetics Module

The solution for the electromagnetic fields requires knowledge of the plasma conductivity, which is obtained from the other modules. The EMM provides time-harmonic azimuthal electromagnetic fields, and it provides the static magnetic fields generated by the permanent magnets or by equivalent dc loops, that is, currents that change on time scales which are long compared to the time in which the plasma reaches quasi-equilibrium.

The EMM module calculates the spatially dependent azimuthal electric fields by solving Maxwell's equation under time harmonic conditions. Assuming azimuthal symmetry, Maxwell's equation for electric fields is reduced to

$$-\nabla\cdot\frac{1}{\mu}\nabla E_\phi = \omega^2\varepsilon E_\phi - i\omega J_\phi, \tag{2.1}$$

where μ is the permeability, E_ϕ is the azimuthal electric field, ω is the frequency of the source current, ε is the permittivity, and J_ϕ is the total current consisting of driving and conduction currents. The conduction current J_c is calculated from $J_c = \sigma E_\phi$, where σ is the conductivity or by explicitly calculating electron currents in the EMCS[11]. At pressures where the electrons are sufficiently collisional, the conductivity of the plasma is

$$\sigma = \frac{q_e^2 n_e}{m_e}\frac{1}{\nu_{me} + i\omega}, \tag{2.2}$$

where q_e is the unit electron charge, n_e represents electron density, m_e denotes electron mass, ν_{me} is the momentum transfer collision frequency of electrons, and ω is the driving frequency. Maxwell's equations are solved using the method of successive over relaxation (SOR). The weighting coefficients and the convergence criterion for the SOR are adjustable simulation parameters.

The static magnetic fields are solved in the radial and axial directions assuming azimuthal symmetry. Under these conditions, the magnetic field can be represented as a vector potential which has only a single component in the ϕ direction. The current loops, which provide source terms when solving for vector potential **A**, by differentiation, yields the static magnetic fields

$$\nabla \times \mathbf{A} = \mathbf{B}; \quad \nabla \times \frac{1}{\mu} \nabla \times \mathbf{A} = \mathbf{j}, \tag{2.3}$$

where μ is the permeability, and **j** is the current density of the source current loops. The vector potential is solved as a boundary value problem using SOR, with the same convergence criteria as the electric field.

A circuit module (CM) is included in the EMM which models a matchbox circuit as well as the coils. The impedance of the matchbox is matched to the coil impedance, allowing the deposited power to be maximized. The source voltage is also adjusted from iteration to iteration allowing the power specified by the input file to be matched and maintained.

2.2.2 The Fluid Kinetics Module

In the FKM, the continuum transport equations for the gas species are solved simultaneously with the electrostatic potential to determine the spatial distribution of species densities as well as the momentum flux fields within the reactor. To solve for these plasma properties, the electron transport properties and the chemical reaction rates are obtained from the EETM. Ion and neutral transport coefficients are obtained from a database or by using Lenard-Jones parameters. To self consistently consider the electrostatic fields, either Poisson's equation can be included, or quasi-neutrality allowing ambipolar fields can be assumed. The continuity equation for all species is

$$\frac{\partial N_i}{\partial t} = -\nabla \cdot \Gamma_i + S_i \tag{2.4}$$

which can be used to solve for the species densities where N_i, Γ_i, and S_i are the respective density, flux, and sources for species *i*.

The electron flux Γ_i is determined by the drift diffusion equation

$$\Gamma_i = \mu_i q_i N_i \overline{E}_s - D_i \nabla N_i \tag{2.5}$$

where μ_i is the mobility of species *i*, D_i is the diffusion coefficient, q_i is the species charge in units of elementary charge, and E_s is the electrostatic field. In this work, we instead used the Scharfetter-Gummel discretization for fluxes.[12] In this method the flux $\vec{\varphi}_{i+\frac{1}{2}}$ between density mesh points (i, i+1) separated by Δx is given by

$$\vec{\varphi}_{i+\frac{1}{2}} = \frac{\alpha \overline{D}(n_{i+1} - n_i \exp(\alpha \Delta x))}{1 - \exp(\alpha \Delta x)} \tag{2.6}$$

where

$$\alpha = -q\overline{\mu}\left(\frac{\Phi_{i+1} - \Phi_i}{\Delta x}\right) \tag{2.7}$$

and $\overline{D}$ and $\overline{\mu}$ are the average diffusion coefficient and mobility in the interval. The ion and neutral flux calculation can be performed using the drift diffusion equation or by including the effects of momentum by the replacement of the diffusional term with terms for pressure, advection, and collisionality:

$$\frac{\partial \Gamma_i}{\partial t} = -\frac{1}{m_i}\nabla(N_i k T_i) - \nabla\cdot(N_i \bar{v}_i \bar{v}_i) + \frac{q_i}{m_i} N_i \bar{E} - \sum_j \frac{m_j}{m_i + m_j} N_i N_j (\bar{v}_i - \bar{v}_j)\nu_{ij} \qquad (2.8)$$

where T_i is the species temperature, $\bar{v}_i$ is the species velocity given by Γ_i / N_i, and ν_{ij} is the collision frequency between specie *i* and specie *j*. The viscosity is included for neutrals only. The gas and ion temperatures are determined from the energy equation for each species:

$$\begin{aligned}\frac{\partial N_i c_v T_i}{\partial t} &= \nabla.\kappa_i \nabla T_i - P_i \nabla.\vec{v}_i - \nabla.(\vec{\varphi}_i \varepsilon_i) + \frac{N q_i^2}{m_i \nu_i} E_s^2 + \frac{N q_i^2 \nu_i}{m_i(\nu_i + \omega^2)} E^2 \\ &+ \sum_j 3\frac{m_{ij}}{m_i + m_j} N_i N_j R_{ij} k(T_j - T_i)\end{aligned} \qquad (2.9)$$

where N_i is the density of specie *i*, c_v is specific heat, T_i is the species temperature, κ_i is the thermal conductivity of specie *i*, P_i is the partial pressure of specie *i*, $\vec{v}_i$ is the specie velocity, $\vec{\varphi}_i$ is the flux of specie *i*, ε_i is the internal energy of specie *i*, E_s is the electrostatic field, E is the RF field, m_i is the mass of specie *i*, m_{ij} is the reduced mass, ν_i is the momentum transfer collision frequency for specie *i*, and R_{ij} is the collision frequency for the collision process between specie *i* and specie *j*.

Time-dependent electrostatic fields are obtained either by solution of Poisson's equation or based on quasi-neutrality allowing an ambipolar approximation. Poisson's equation is given by

$$-\nabla\cdot\varepsilon\nabla\Phi^{t+\Delta t} = \rho^{t+\Delta t} \qquad (2.10)$$

where ε is the permittivity, $\Phi^{t+\Delta t}$ is the electric potential at time $t + \Delta t$, and $\rho^{t+\Delta t}$ is the net charge density at time $t + \Delta t$. Poisson's equation is calculated semi-implicitly by approximating the charge density linearly as

$$\rho^{t+\Delta t} = \rho^{t} + \Delta t \cdot \left.\frac{\partial \rho}{\partial t}\right|^{t+\Delta t} \tag{2.11}$$

where $\rho^{t+\Delta t}$ is the charge density at time $t+\Delta t$, and ρ^{t} is the charge density at time t. The evolution rate of the charge density $\partial\rho/\partial t$ is determined by the divergence of the total current density $\mathbf{j}$:

$$\frac{\partial \rho}{\partial t} = -\nabla \cdot \mathbf{j} + S\,, \tag{2.12}$$

where S is the source function of charges. When using drift-diffusion, in the plasma region, $\mathbf{j} = \mathrm{q_i}(-\mathrm{D_i}\nabla \mathrm{n_i} + \mathrm{q_i}\mu_\mathrm{i}(-\nabla\phi))$ for electrons and $\mathbf{j} = \mathrm{q}\Gamma$ for ions. When using Scharfetter-Gummel fluxes, $\mathbf{j} = f(\Phi, N)$, and so:

$$\frac{\partial \rho}{\partial t} = -\nabla \cdot \left(\mathbf{j} + \frac{\partial \mathbf{j}}{\partial \Phi}\Delta\Phi + \frac{\partial \mathbf{j}}{\partial N}\Delta N \right) + S \tag{2.13}$$

In materials, $\mathbf{j} = \sigma(-\nabla\phi)$ where σ is the material conductivity. By making the potential fully implicit in this scheme while using explicit terms for the assumedly more slowly varying

species properties such as density and temperature, the time step used in the SOR solution can be lengthened beyond the dielectric relaxation time and greatly accelerate solution over the fully explicit formulation.

The second option is to compute electrostatic fields using a quasi-neutrality approximation over the entire plasma region. Under such an assumption the electron density can be set equal to the total ion density at all locations. To maintain this charge neutrality requires that

$$-\nabla \cdot \Gamma_e + S_e = \sum_i q_i(-\nabla \cdot \Gamma_i + S_i) \tag{2.14}$$

or

$$\nabla \cdot (\mu_e n_e \nabla \phi + D_e \nabla n_e) + S_e = \sum_i q_i(\nabla \cdot (-\mu_i n_i \nabla \phi + D_i \nabla n_i) + S_i) \tag{2.15}$$

where S_e and S_i represent electron and ion source functions, respectively, due to both internal and external sources such as electron beams. The flux terms are replaced by their drift diffusion approximations and the terms are rearranged to get

$$\sum_i q_i \nabla \cdot \left(q_i n_i \mu_i \nabla \phi - D_i \nabla n_i\right) = \sum_i q_i S_i \tag{2.16}$$

where the summations are taken over all charged species including both electrons and ions. By reducing the system to a steady-state solution, the dielectric relaxation time is removed as a limit allowing much larger time steps to be taken, which are limited only by the Courant limit.

A semi-analytic sheath model (SM) has also been integrated with the FKM to represent the fields and fluxes at gas-solid boundaries under conditions where the actual sheath thickness is

less than the mesh spacing. A multi-species form of Riley's unified sheath model[12] is used to relate the sheath charge Q and boundary conditions to the potential drop. This potential drop across the sheath produced by the semi-analytic sheath model is then applied as a jump condition at plasma wall boundaries in solving Poisson's equation for the entire reactor.

2.2.3 The Electron Energy Transport Module

In the Electron Energy Transport Module, the power deposition into the electrons, as well as the electron impact sources, are modeled and the electron transport properties are computed. These can be solved in two different ways. The first method is to solve the 2d electron energy equation. Electron transport properties as a function of temperature are obtained by solving the 0d Boltzmann equation. The second method is to utilize a Monte Carlo simulation, in which electron pseudo-particles are moved in the computed fields and have collisions with the other plasma species. The trajectories are integrated over a period of time and the statistics are collected to generate the electron energy distribution functions (EEDs), which are then used to calculate the rate coefficients.

2.2.3.1 The Electron Energy Equation Method

When solving the electron energy equation the 0d Boltzmann equation is solved for a range of values of electric field divided by total gas density (E/N) in order to create a lookup table correlating average energy with a transport coefficient. The Boltzmann equation is expressed as

$$\frac{\partial f_e}{\partial t} + \mathbf{v} \cdot \nabla_{\mathbf{r}} f_e - \frac{e(\mathbf{E} + \mathbf{v} \times \mathbf{B})}{m_e} \cdot \nabla_{\mathbf{v}} f_e = \left(\frac{\delta f_e}{\delta t} \right)_{collision}, \tag{2.17}$$

where $f_e = f_e(t, \mathbf{r}, \mathbf{v})$ is the electron distribution function, ∇_r is the spatial gradient, ∇_v is the velocity gradient, m_e is the electron mass, and $\left(\frac{\delta f_e}{\delta t}\right)_{collision}$ represents the effect of collisions. The resulting values are then used as a lookup table, which yields electron mobility, thermal conductivity, energy-loss rate due to collisions and electron impact rate coefficients as a function of electron temperature. T_e is defined as 3/2 <ε>, where <ε> is the average energy computed from the EEDs.

With the EEDs known as a function of temperature, the steady state electron energy equation is solved as follows

$$\nabla \kappa \nabla T_e + \nabla \cdot (\Gamma_e T_e) = P_h - P_l \ , \tag{2.18}$$

where κ is the thermal conductivity, T_e is the electron temperature, Γ_e is the electron flux, P_h is the electron heating due to deposition, and P_l is the power loss due to inelastic collisions. The electron flux Γ is computed in the FKM, and the power deposition rate is computed from the time-averaged value of $\mathbf{j} \cdot \mathrm{E}$, where $\mathbf{j} = q\phi_e$. The electric field includes both the inductive field computed in the EMM and the electrostatic field computed in the FKM. The above equation is discretized and solved by SOR, with the transport coefficients updated based on the local electron temperature.

Alternatively, the electron energy equation can be implicitly integrated in time in the FKM to provide electron temperature, and impact and transport coefficients.

2.2.3.2 The Electron Monte Carlo Method

The Monte Carlo method is a fully kinetic treatment, which resolves the transport of electrons in electric and magnetic fields using a semi-implicit technique. Noncollisional heating can be kinetically resolved by producing electron currents, which are used to correct the assumption of collisional power deposition in the EMM.

The Electron Monte Carlo Simulation (EMCS) tracks the trajectory of electron pseudo-particles by moving them in the computed electric and magnetic fields as a function of time. A group of electrons is initialized from a Maxwellian distribution and randomly distributed within the rf period (when using harmonic fields), with starting locations randomly determined within the reactor volume weighted by the electron density computed in the FKM. The electron energy range is divided into discretized energy bins for collision determination and this binning also helps in collecting statistics. The collision frequency ν_i within any energy bin is computed by summing all possible collision within the energy range

$$\nu_i = \left(\frac{2\varepsilon_i}{m_e}\right)^{\frac{1}{2}} \sum_{j,k} \sigma_{ijk} N_j \qquad (2.19)$$

where ε_i is the average energy within the bin, σ_{ijk} is the cross section at energy *i,* for species *j* and collision process *k*, and N_j is the number density of species *j*. The time between the collisions is randomly determined using the maximum collision frequency for all energy bins. $\Delta t = \frac{-1}{\upsilon}\ln(r)$, r= (0,1). At the time of a collision, the reaction that occurs is chosen randomly from all the possible reactions for that energy bin. A null collision cross section makes up the difference between the actual collision frequency and the maximum collision frequency at any given spatial

location. In this work electron-electron collisions are not considered. The velocity of the electrons is adjusted based on the type of collision it undergoes. If the collision is null then the electron's trajectory is unaltered. Particle trajectories are integrated using the Lorentz equation.

$$\frac{d\bar{v}}{dt} = \frac{q_e}{m_e}\left(\bar{E} + \bar{v} \times \bar{B}\right) \tag{2.20}$$

and

$$\frac{d\bar{r}}{dt} = \bar{v} \tag{2.21}$$

where $\bar{v}$, $\bar{E}$, and $\bar{B}$ are the electron velocity, local electric field, and magnetic field respectively. Eq. (2.20) and (2.21) are updated using a second-order predictor corrector scheme. Electric fields are both the inductive fields computed in the EMM and the time-dependent electrostatic fields computed in the FKM. Time steps are chosen to be less than both 1% of the rf period and 1% of the cyclotron frequency, and small enough that the particles do not cross more than one-half computational cell in one time step. Several hundred to a few thousand particles are integrated in time for many rf cycles, typically greater than 100 rf cycles.

The statistics for computing the electron energy distributions (EEDs) are updated every time an electron is moved in the mesh, which is at every time step using finite particle techniques. These statistics are collected into an array for energy *i* and location *l*.

$$F_{il} = \sum_j w_j \delta((\varepsilon_i \pm 1/2\ \Delta\varepsilon_i) - \varepsilon_j)\delta((\vec{r}_l \pm \Delta\vec{r}) - \vec{r}_j) \tag{2.22}$$

where the summation is over particles, w_j is the weighting of the particle, ε_i is the energy and r_k is the bin location. The weighting w_j is a product of three factors; the relative number of electrons each pseudo-particle represents, the time step used to advance the trajectory, and a spatial weighting obtained using the method of finite-sized particles (FSP). At the end of the EMCS, the electron temperature, collision frequency and electron-impact rate coefficients are computed as a function of position from the EEDs. The EEDs f_{ik} are obtained from the raw statistics F_{ik} by requiring normalization of each spatial location.

$$\sum_i F_{ik} \Delta\varepsilon_i = \sum_i f_{ik} \varepsilon_i^{\frac{1}{2}} \Delta\varepsilon_i = 1 \tag{2.23}$$

The electron temperature is defined by convention to be 2/3 <ε>. The electron impact rate coefficient (k_m) for electron impact process *m* and location *l* is computed as

$$k_{ml} = \int_0^\infty \left(\frac{2\varepsilon}{m_e}\right)^{\frac{1}{2}} \sigma_m(\varepsilon) f_l(\varepsilon) \varepsilon^{\frac{1}{2}} \, d\varepsilon = \sum_i \left(\frac{2\varepsilon_i}{m_e}\right)^{\frac{1}{2}} \sigma_{mi} f_{il}(\varepsilon) \varepsilon_i^{\frac{1}{2}} \Delta\varepsilon \tag{2.24}$$

2.2.4 The Plasma Chemistry Monte Carlo Module

To obtain the energy and angular distributions of reactive species to the substrate, the PCMCM was developed for the HPEM. The PCMCM calculates the trajectories of plasma species in the gas phase and their collisions with surfaces. This module was originally a postprocessor to the HPEM. It used volumetric sources of plasma species, time-dependent electric fields, and sheath properties exported from the HPEM to obtain the angular and energy

distributions of the fluxes using Monte Carlo techniques.[10] The PCMCM functions in a similar manner but also accounts for nonthermal, or in-flight fluxes, resulting from sputter sources in addition to the volumetric sources. Sputtered atoms and neutralized ions which are reflected from the target have kinetic energies of several eV. These species are not initially in thermal equilibrium with the buffer gas which has a temperature of ≤0.3 eV. Under certain process conditions, these energetic particles may not thermalize prior to reaching the wafer. The trajectories and energies of these nonequilibrium particles are already tracked by the sputter algorithms in the FKM. Statistics on the energy and angular distributions of the particles as they strike selected surfaces are collected and passed to the PCMCM.

Based on these quantities, a rate of generation of species *i* as a function of position, $G_i(\vec{r})$ ($cm^{-3}s^{-1}$), is computed. This generation term accounts for all sources of species *i* on the right-hand side of reactions in the mechanism. The rate $G_i(\vec{r})$ also includes source functions on surfaces due to, for example, sputtering. In a similar fashion, a consumption rate $C_i(\vec{r})$ ($cm^{-3}s^{-1}$) is computed based on all reactions containing species *i* on the left-hand side of reactions in the mechanism. A local elastic collision frequency with each species is also computed. These elastic frequencies are added to the local consumption frequency $C_i(\vec{r})\Delta V(\vec{r})$ $\Delta V(\vec{r})$ is the volume of the computational cell at location $\vec{r}$ to yield a total interaction frequency $\nu_T(\vec{r})$. Null collision techniques are used at each spatial location to provide a reactor wide collision frequency ν_i for each species *i*.

Pseudoparticles of species *i* are launched from each computational cell at a time randomly chosen in the rf cycle with a weighting (or total number) proportional to

$G_i(\vec{r})\Delta V(\vec{r})$. The velocity is randomly chosen from a Maxwell-Boltzmann distribution having a local temperature $T_i(\vec{r})$ for volumetric sources where the spatially dependent temperature for each species is computed by HPEM. The trajectories of the pseudoparticles are integrated for the time

$$\Delta t = -\frac{1}{\nu_i}\ln(r), \tag{2.25}$$

where Δt is the time step for movement of the pseudoparticle and r is a random number distributed on (0,1). For ions, acceleration by the local electric field is accounted for. The time step used to increment the trajectory is limited by the time required to cross a specified fraction of the cell (typically 0.2). For ions, additional constraints are applied including a specified fraction of the rf cycle (typically 0.05), or the time to cross a specified fraction of the sheath width (typically 0.01).

At the end of the time step, Monte Carlo techniques are use to determine if the collision is real or null. If real, another random number is used to determine if the collision is elastic or consuming. If consuming, the particle is removed from the simulation. If elastic, the collision partner is identified using another random number and the velocity of the pseudoparticle is changed appropriately using standard elastic collision techniques. The one exception is for charge exchange collisions which are separately accounted for in the sum of collision frequencies. If an ion undergoes a charge exchange collision, its identity is changed to the neutral counterpart and the trajectory is retained. The trajectories are advanced until the

pseudoparticles reach the vicinity of a surface. If the surface is chosen as one for which statistics on incident species are desired, ions are then integrated through the sheath, a computationally expensive process. For surfaces not selected, the particles are removed from the simulation. A similar process is followed for the neutrals, except for integration through the sheath.

2.3 Figures

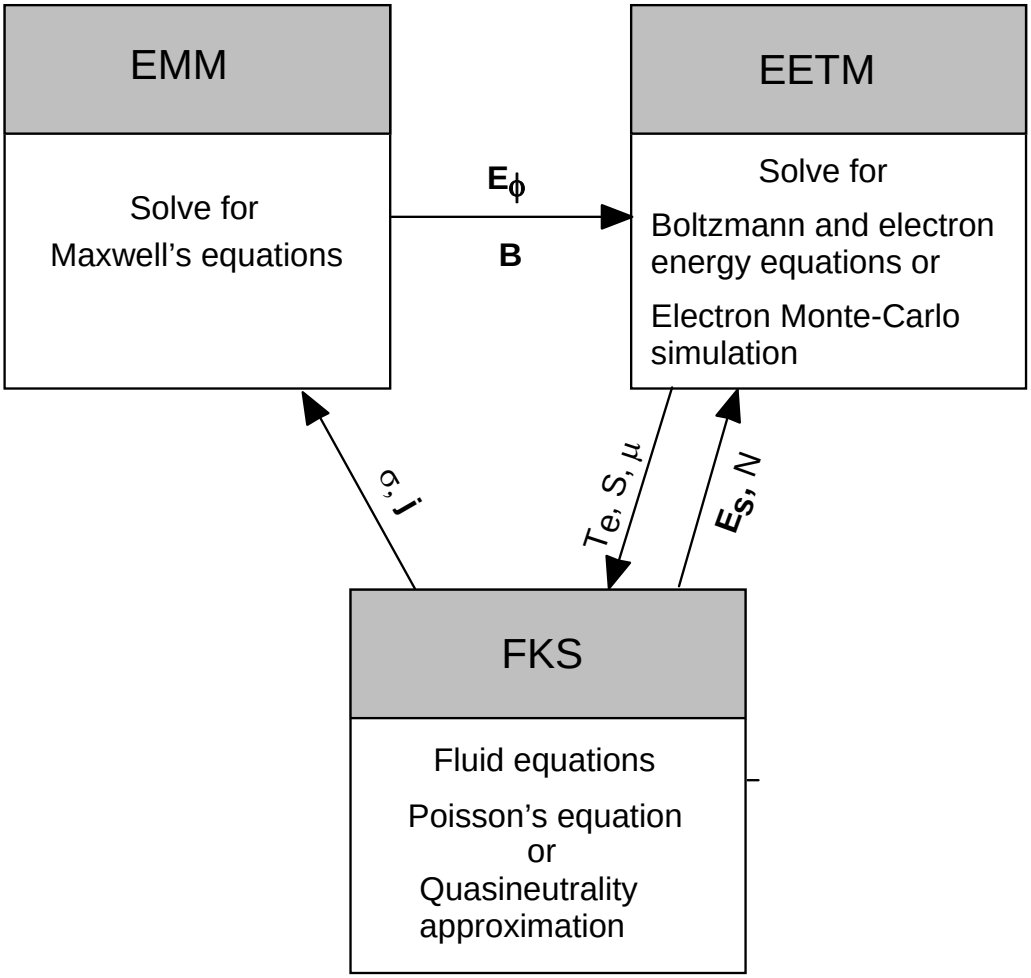

Fig. 2.1. Schematic of the modular HPEM

2.2 References

[1] P. L. G. Ventzek, R. J. Hoekstra and M. J. Kushner, J. Vac. Sci. Techno. B **12**, 416 (1993)

[2] W. Z. Collison and M. J. Kushner, Appl. Phys. Lett. **68**, 903 (1996)

[3] M. J. Kushner, W. Z. Collison, M. J. Grapperhaus, J. P. Holland, and M. S. Barnes, J. Appl. Phys. **80**, 1337 (1996)

[4] M. J. Grapperhaus and M. J. Kushner, J. Appl. Phys. **81**, 569 (1997)

[5] S. Rauf and M. J. Kushner, J. Appl. Phys. **81**, 5966 (1997)

[6] R. L. Kinder and M. J. Kushner, J. Vac. Sci. Technol. A **19**, 76 (2001)

[7] J. Lu and M. J. Kushner, J. Appl. Phys. **87**, 7198 (2000)

[8] A. Sankaran and M. J. Kushner, J. Appl. Phys. **92**, 736 (2002)

[9] J. Lu and M. J. Kushner, J. Vac. Sci. Technol. A **19**, 2652 (2001)

[10] R. J. Hoekstra, M. J. Grapperhaus, and M. J. Kushner, J. Vac. Sci. Technol. A **15**, 1913 (1997)

[11] S. Rauf and M. J. Kushner, J. Appl Phys. **81**, 5966 (1997)

[12] D. L. Scharfetter and H. K. Gummel, IEEE Transactions on Electronic Devices **ED-16**, 64 (1969).

[13] M. E. Riley, *Sandia Report SAND 95-0775. UC-401*, 1995

3. MONTE CARLO FEATURE PROFILE MODEL

3.1. Introduction

The Monte Carlo Feature Profile Model (MCFPM) has been developed to allow self-consistent determination of topographical feature evolution for semiconductor processing in plasma reactors.[1-3] To date, the model has been focused on etching, stripping and ionized metal physical vapor deposition (IMPVD), but has the generality and capability to include other processes such as plasma enhanced chemical vapor deposition (PECVD) and physical vapor deposition (PVD). The MCFPM is integrated with the Hybrid Plasma Equipment Model (HPEM) through the use of energy and angular distributions (EADs) produced by the Plasma Chemistry Monte Carlo Module (PCMCM) in the HPEM for arbitrary radial locations on the substrate.

The MCFPM is described in Section. 3.2. The computation mesh used in the MCFPM and the algorithms for particle motion is presented in Section. 3.2.1. The physics of the interaction of energetic particles with the surface is captured in Section. 3.2.2. The surface diffusion algorithm used for deposition process is described in Section. 3.2.3. The surface reaction mechanisms used in this work for fluorocarbon etching of SiO_2/Si substrates are discussed in Section 3.3.

3.2. Description of the Model

The MCFPM is a Monte Carlo model, which simulates the use of statistically weighted pseudoparticles representative of the fluxes of active species to the feature surface. Through ballistic transport and interaction with the mesh delineated surface, time integrated surface evolution is obtained.

3.2.1. Computational mesh and particle motion

The MCFPM resolves wafer features (masks, photoresists, semiconductors) on the submicron scale utilizing a rectilinear mesh. The mesh spacing in typically $\approx 1 \times 1$ nm , which is $\approx 4 \times 4$ or fewer atoms. Each cell is assigned a material identity (e.g., poly-Si, photoresist, SiO_2, plasma) which may change during the simulation. Solid species, including adsorbates or passivation, are represented by the identity of the computational cell. Gas phase species (i.e., radicals and ions) are represented by computational pseudoparticles. Pseudo-particles are launched towards the surface from random locations above the trench with energies and angles sampled from the EADs obtained from the PCMCM. The EADs produced by the PCMCM are flux weighted probability distribution functions (F) which must be converted and normalized as cumulative distribution functions (f).

$$f(\varepsilon , \theta, r) = \frac{F(\varepsilon , \theta, r)}{\int \int F((\varepsilon , \theta)\, d\varepsilon\, d\theta} \tag{3.1}$$

The pseudoparticles are launched with a frequency computed from the total flux of radicals or ions incident onto the substrate so that each pseudoparticle represents a fraction of the number of atoms in a mesh cell based on the gas-to-material weighting ratio.

$$W_g = \frac{1}{\gamma} W_s \tag{3.2}$$

where W_g is the gas particle weighting, W_s is the mesh or surface cell weighting, and γ is the gas-to-surface ratio, which was set to 1 for this work. The pseudoparticle trajectories are advanced in time where the calculation of position and velocity are separated allowing solution of two linear equations:

$$v_i = v_{i-1} + \frac{qE}{m}\Delta t \text{ and } x_i = x_{i-1} + v_i \Delta t \tag{3.3}$$

where v and x represent the velocity and position of the particle, and the subscripts indicate the former or current velocity and position; q and m indicate the charge and mass of the particle, respectively; and Δt indicates the time-step taken by the particle. This method is used because under the majority of cases the effects of charging are ignored and the electric field E is set to zero, allowing solution of the second linear equation only. Particle motion can be sequenced in the following steps.

1. At any instant of the particle's motion, the time step for its current move is determined by the time required to move the minimum distance to a surface.

2. Based on this time step and the solution to Eq. 3.3, the new velocity and position of the particle is determined. At this point the time step is reset so that the next move can be performed.

3. If the distance to a surface is still greater than one mesh cell, this new distance is used to calculate the time step for the next move and step 2 is repeated. The particle is thus moved until a material containing cell is occluded.

4. Only for $\gamma > 1$, if the particle is within one mesh cell of a surface, the particle is moved back to its previous position, the previous time-step is halved, and the particle is moved again. This process is iterated until the particle moves within a fraction of the material containing cell, generally $0.05 \times$ (Cell Width).

The effects of surface charging on the profile evolution can be addressed. Electron trajectories can be simulated as low-temperature isotropic fluxes which impinge upon the feature during the low-potential swing of the sheath. This macroscopically balances the current due to the ions. To resolve the electric fields due to the charged surfaces of the feature, an iterative explicit solution of Poisson's equation is determined utilizing successive overrelaxation (SOR).

$$\nabla \cdot \varepsilon \nabla \varphi^{t+\Delta t} = -\rho^{t} \tag{3.4}$$

SOR is used to accelerate solution by multiplying the calculated $\Delta\phi$ by an overrelaxation factor greater than one. Neumann boundary conditions are used at the top and bottom of the feature by assuming that the electric field above the feature matches the sheath field from the fluid-chemical kinetics module (FKM) and that the electric field below the feature is approximately zero. The left and right boundaries are assumed to follow a periodic Dirichlet condition.

3.2.2 Energetic particle interaction

The specifics of the interaction of energetic particles with surface species are determined by the EADs. The source of energetic particles is ions accelerated through the sheath, with energies of up to 100s eV and angular spreads <5-10° from the vertical. We have assumed that

ions neutralize upon interaction with the surface and so do not distinguish between energetic ions and energetic neutrals. Energetic particles can either specularly or diffusively reflect from surfaces, with an energy loss which is larger for diffusive scattering and small for specular.

Following the work of Donnelly *et al* and Graves *et al*, our generalized reaction probability for a particle of energy E incident onto a surface at an angle θ from the local vertical of the surface is [4,5]

$$p(\theta) = p_0 \left[\frac{E^n - E_{th}^n}{E_r^n - E_{th}^n} \right] f(\theta), \tag{3.5}$$

where E_{th} is the threshold energy of the process, E_r is a reference energy, p_0 is the probability for normal incidence at E_r and $f(\theta)$ is the relative probability at angle of incidence θ. Based on the work of Graves *et al* $f(\theta)$ is an empirical function typical of chemically enhanced sputtering with a maximum value near $\theta = 60°$.[5]

The reflection of particles from surfaces was given both specular and diffusive character. To account for surface roughness on spatial scales not resolved by our model, we specified that a fraction $f_d = 0.25$ was diffusively scattered. The energy of specularly reflected particle was scaled such that forward scattered particles retain the majority of their energy. The specularly reflected particle energy for incident energy E_I is

$$E_s(\theta) = E_I \left(\frac{E_I - E_c}{E_{ts} - E_c} \right) \left(\frac{\theta - \theta_c}{90° - \theta_c} \right) \tag{3.6}$$

for $\theta > \theta_c$, $E_c < E_I < E_{ts}$. Particles having $\theta < \theta_c$ or $E_I < E_c$ are said to diffusively scatter. Particles having $E_I > E_{ts}$ are said to retain all of their energy subject to the angular correction. We used E_{ts} = 100 eV, E_c = 0 eV and θ_c = 60°. The final reflected energy of the particle is a weighted sum of the specularly reflected energy and diffusively reflected energy.

The construction of the probability arrays for interaction of gas phase with surface cells is problematic due to the energy dependence of the reaction probability and the requirement that probabilities add to unity. This process is facilitated by use of a null process for all combinations of incident gas phase species and surface species. The null process is reflection without reaction. As the probability of energy dependent process change, the null portion of the probability array is rescaled to ensure that the sum of probabilities is unity. Should an etch yield exceed unity, the null reaction is eliminated and array rescaled.

3.2.3 Surface Diffusion

The MCFPM is also capable of addressing surface diffusion during deposition of materials.[3] We only used this option for diffusion of metal atoms on metal underlayers. All depositing metal atoms are first physisorbed, which are treated differently from the underlying material even if they have the same composition. The physisorbed atoms diffuse on the surface before they are chemisorbed onto the underlying material. An adsorbed cell can diffuse into any unoccupied adjacent cell in the mesh. The probability that an adsorbed cell i moves to another cell j is dependent on their potential energy values, which are based on effective Morse potentials.

$$\Phi_{ij} = \Phi_0 \left\{ \exp\left(-2\,\frac{r_{ij} - r_0}{a_0} \right) - 2\exp\left(-\frac{r_{ij} - r_0}{a_0} \right) \right\} \tag{3.7}$$

where r_{ij} is the distance between the center of the cells. Φ_0 was set to 0.3 eV based on the predictions by Lu *et al*.[3] r_0 and a_0 were set to 1.6 nm and 5 nm based on mesh scale lengths as opposed to atomic lengths. The probability of diffusion to all possible locations is summed and normalized. The final diffusion path is then chosen randomly. Based on the chosen value of the activation energy for diffusion from i to j (E_{ij}), the adsorbed cell either chemisorbs or diffuses. The frequency of such trials is governed by the jump frequency ν,

$$\nu = -\nu_{ij} \ln(r) \tag{3.8}$$

where

$$\nu_{ij} = \nu_0 \exp\left(-\frac{E_{ij}}{k_b T_s} \right) \tag{3.9}$$

and

$$\nu_0 = 2k_b T_s / h \tag{3.10}$$

where h is the Planck's constant, k_b is the Boltzman's constant and T_s is the substrate temperature. At 393 K, $\nu_0 = 1.6 \times 10^{12}$ s^{-1}. Based on the specified threshold jump frequency (ν_t), the cell chemisorbs if $\nu<\nu_t$. ν_t was chosen to be 10^8 s^{-1} based on earlier studies.[3]

3.3 Surface Reaction Mechanisms

Surface reaction mechanisms, in general, are an intrinsic property of the gas phase reactant species (incident on the surface) and the surface species. As such reaction mechanisms should be independent of the process conditions, such as the plasma source or the gas chemistry. The process conditions may determine the energies and magnitudes of the incident reactant fluxes, however the reaction mechanism should not itself. The reaction mechanism for etching of SiO_2 and Si in fluorocarbon plasmas is schematically shown in Fig. 3.1 and is listed in Appendix A.[6]

3.4 Figures

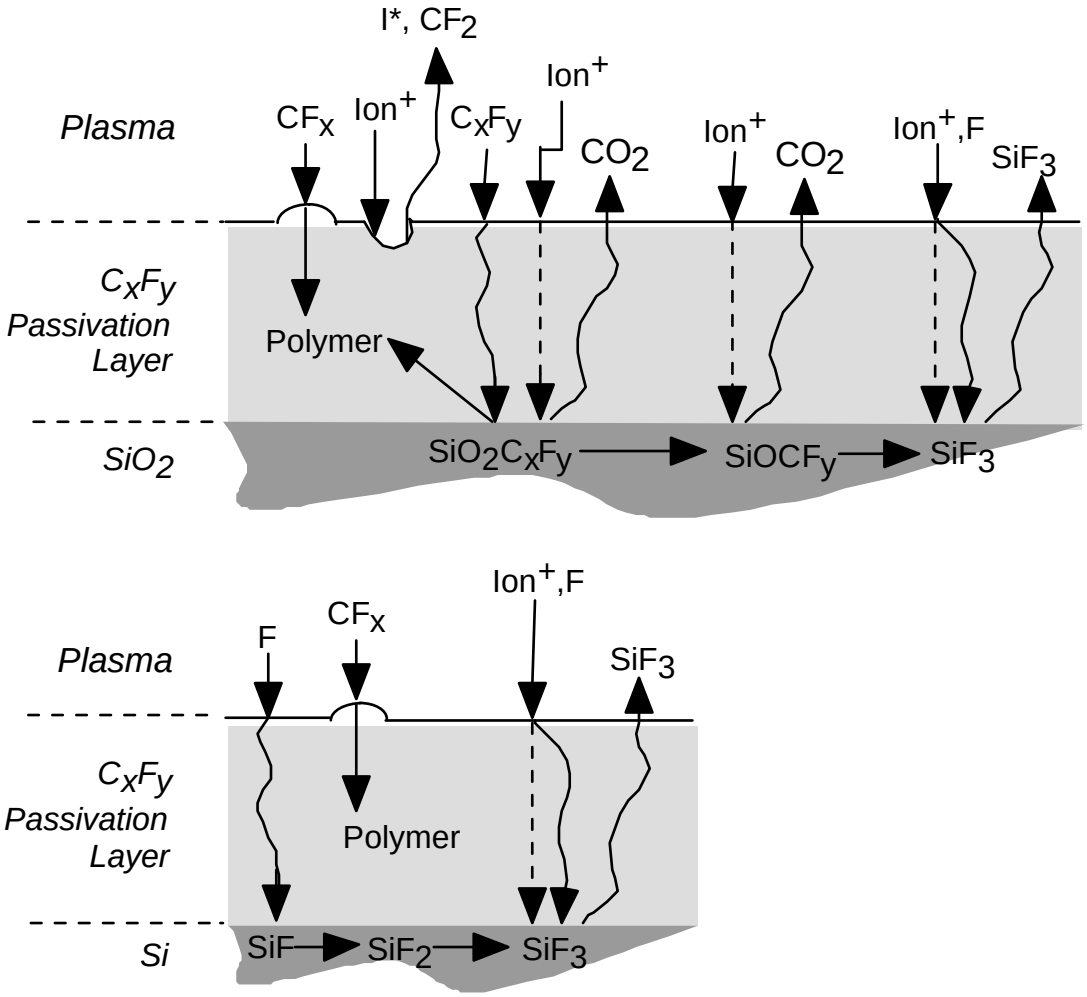

Fig. 3.1. Schematic of surface reaction mechanism for fluorocarbon etching of SiO_2/Si. I^+ refers to an ion. I* refers to a hot neutrals. The dashed lines represent energy transfer through the polymer. The curved lines represent species diffusion through the polymer.

3.5 References.

[1] R. J. Hoekstra, M. J. Grapperhaus, and M. J. Kushner, J. Vac. Sci. Technol. A **15,** 1913 (1997).

[2] R. J. Hoekstra and M. J. Kushner, J. Vac. Sci. Technol. B **16,** 2102 (1998).

[3] J. Lu and M. J. Kushner, J. Vac. Sci. Technol. A **19,** 2652 (2001).

[4] C. C. Cheng, K. V. Guinn, V. M. Donnelly, and I. P. Herman, J. Vac. Sci. Technol. A **12,** 2630 (1994).

[5] C. F. Abrams and D. B. Graves, J. Appl. Phys. **86,** 2263 (1999).

[6] A. Sankaran and M. J. Kushner, J. Vac. Sci. Technol. A **22,** 1242 (2004).

4. EFFECT OF NON-SINUSOIDAL BIAS WAVEFORMS ON ION ENERGY DISTRIBUTIONS AND FLUOROCARBON PLASMA ETCH SELECTIVITY

4.1. Introduction

In this chapter the effect of tailored voltage bias waveform selected on the shape of the IED and etch characteristics obtained are investigated and the results are presented. The model system is an inductively coupled plasma (ICP) reactor operating in an Ar/*c*-C_4F_8 gas mixture etching SiO_2 over Si. The narrow IED was used to achieve high etch selectivity of SiO_2 over Si by positioning the peak of the IED by either varying the shape of the voltage waveform or the voltage amplitude. An etching recipe based on varying the amplitude of the tailored voltage waveform was designed which results in a high etch selectivity at high rate without changing the gas chemistry.

4.2. Base Case Conditions

The model system is an ICP reactor schematically shown in Fig. 4.1. Inductive power is supplied through a 3-turn coil, 16 cm in diameter. The coil sits on a 2 cm thick quartz window which is 23 cm in diameter. The wafer is on a substrate, which can be independently biased, 7 cm below the quartz window. For the base case, a 15 mTorr Ar/*c*-C_4F_8=75/25 gas mixture was used which enabled investigation of the effect of rf bias voltage on both high and low mass ions. For the base case, the flow rate was 100 sccm, the coil source was powered at 5 MHz and delivered a purely inductive power of 500 W. The shape and amplitude of the rf bias waveform will be varied at the electrode. The reaction mechanism for Ar/*c*-C_4F_8 mixtures is given in Appendix B[1].

The tailored non-sinusoidal bias voltage waveform used in this work is shown in Fig. 4.2. This voltage waveform consists of a quasi-dc negative bias to accelerate positive ions through the sheath with a narrow positive excursion to attract electrons and so balance the positive flux. The quasi-dc bias produces a nearly constant sheath potential as a function of time during the rf cycle which, if unperturbed by the positive voltage spike, would produce a narrow IED.[2] If the positive going excursion is of short enough duration, the heavy ions are unable to respond to the change in sheath potential and the perturbation to the narrow IED is minimal. The voltage waveforms have been characterized on the basis of the fraction of the time that the voltage is positive in one rf cycle, α. Based on this terminology the voltage waveform in Fig. 4.2 is called the "α=10% waveform".

The total positive ion density for the base case (α=10%, 200 V peak-to-peak) is shown in Fig. 4.3. Corresponding radical and ion fluxes to the wafer are shown in Fig. 4.4. The large electron density ($\approx 10^{11}$ cm^{-3}) highly dissociates the *c*-C_4F_8 feedstock. As a result, the major radical fluxes are CF, C_2F_3, and F; and the major ion fluxes consist of Ar^+, CF_3^+, and CF^+. The total ion density peaks at the center of the reactor, as do ion fluxes. This peaking is due, in part to the accumulation of negative ions at the peak of the nearly quasi-dc plasma potential, and the need for a neutralizing positive ion flux. Lower F atom and ion fluxes may result in a thicker passivation layer near the edge of the wafer. The net result of the two opposing effects is that the etch rates near the edge of the wafer are slightly lower than at the center.

Time-averaged IEDs (sum of for all ions) are shown in Fig. 4.5 for α=2% through 12 % waveforms and for a sinusoidal waveform (200 V peak-to-peak, 5 MHz). The sinusoidal voltage waveform produces the familiar broad IED which results from ions of different masses entering the sheath a random times during the rf cycle. The time required for the lighter ions (e.g. F^+,

CF^+) to cross the sheath is commensurate with the rf period and so they arrive at the substrate with nearly the instantaneous sheath potential. The heavier ions (e.g., $C_2F_4^+$) may require many rf periods to cross the sheath, and so arrive with a narrower energy distribution centered on average sheath potential. The end result is a fairly broad IED, in this case extending for 85 eV.

The peak-to-peak voltage for the tailored waveforms is also 200 V at 5 MHz, divided between a –170 V quasi-dc portion and a positive 30 V spike. The tailored waveforms generally produce a narrower IED than the sinusoidal case in large part because the sheath voltage remains constant between the positive going spikes of the bias. The transit time across the sheath for the lighter ions is short compared to the pulse period, so the energy of each ion depends on the instantaneous potential drop when it enters the sheath.[2] As with the sinusoidal bias, the heavier ions may require many rf cycles to cross the sheath, and so arrive at the substrate with an energy more akin to the average sheath potential. If the positive going voltage spike is of sufficiently short duration, the cycle averaged sheath potential does not vary significantly from the quasi-dc sheath potential during the negative portion of the cycle, and so the IED is not significantly broadened. As α increases, the IED broadens since the sheath potential is on the average less negative for a larger fraction of the rf cycle. Note, however, that even for small α there is an intrinsic width to the IED. This width results, in part, from ions arriving at the edge of the sheath with a distribution of the energies upon the value of the plasma potential at the location of their last collision. This spread in energy could be as large as a few times the presheath voltage (10 or 20 eV).

Based on these arguments, the IED should be less sensitive to ion mass than a sinusoidal bias. The sensitivity to mass of the IED using the tailored waveform is demonstrated by the results shown in Fig. 4b. IEDs are shown for F^+ (light) and $C_4F_7^+$ (heavy) for the tailored α=10%

and sinusoidal waveforms. The lighter ion has a broader IED which has a different shape from that of the heavier ion with the sinusoidal waveform. Using the tailored waveform the IED for the lighter ion does gain breadth compared to the heavier ion, though the broadening is still a small fraction of the average energy.

Time-average IEDs for all ions are shown in Fig. 4.7 for α=20% through 75% waveforms (200 V peak-to-peak), and for a sinusoidal waveform. As the duration of the positive portion of the pulse increases, the IEDs broaden in energy and approach forms similar to that of sinusoidal IED. When the waveform exceeds α=50%, the waveform changes from being dominantly cathodic to being dominantly anodic, producing a thinner, lower voltage sheath. The bias begins to appear more like a positive dc bias than an rf bias. As a result, a narrower IED is again observed, albeit with its average energy being lower.

The average applied voltage for the sinusoidal waveform is zero and, for this geometry, the resulting dc self-bias produced by the plasma is negative. The magnitude of this dc bias then adds to the energy of positive ions accelerated down the sheath. The time-averaged voltage for the non-sinusoidal waveform which we are using here is negative. As a consequence, even in the absences of asymmetries in the reactor, the self-generated dc bias will be positive. The self-bias with the tailored waveform decreases towards negative values as the waveform becomes more symmetric and α approaches 50%, as shown in Fig. 4.8. For example, the dc bias for α=2% is 75 V, decreasing to –21 V for α=50%. The increasing average ion energy as α increases, shown in Fig. 4.5, is due in part to this decrease in dc bias towards more negative values. The tailored waveform for α=40% is essentially symmetric. As a result, the dc bias for that waveform should, in principle, differ from the dc bias for sinusoidal waveform by 70 V, the offset voltage. The dc bias is, however, more negative than this expectation. The reason is that the α=40% waveform

has significantly higher harmonic content that the sin wave. These higher harmonics increase the displacement portion of the current, producing a more asymmetric collection of current.

To obtain a high etch selectivity, the width of the IED should be narrow enough so that the energies of the majority of ions striking the substrate fall between the threshold energies for etching the materials of interest. With the tailored waveform, this requirement can be met by varying the voltage amplitude, frequency or α. For example, time-averaged IEDs for the sum of all ions are shown in Fig. 4.9 for α=2% through 12% waveforms and sinusoidal waveform at a repetition frequency of 2 MHz. As is the case for 5 MHz (see Fig. 4.5), the IEDs for the tailored waveform are considerably narrower than the corresponding sin wave bias. The IEDs at the lower frequency are controllably broader than at 5 MHz, affording some amount of tenability to the IEDs.

Time-averaged IEDs for all ions are shown in Fig. 4.10 for α=10% for different peak-to-peak voltages. The positive voltage excursion is 15% of the peak-to-peak voltage for all cases. As expected, the maximum and average energies of the tailored IEDs increase on increasing the peak-to-peak amplitude. In spite of keeping the ramp-up and ramp-down times constant, the IEDs tend to broaden in energy with increasing voltage. This broadening is due, in part, to the thickening of the sheath at higher voltages which then requires longer transit times across the sheath. The residence times of some ions in the sheath therefore statistically overlap with that portion of the cycle that the sheath potential less negative, thereby extending the IED to lower energies. At the highest voltages this thickening results in the sheath becoming mildly collisional. The IEDs at higher voltages are, however, still narrow in energy when compared to the sinusoidal voltage waveform with the same peak-to-peak voltage. The angular width of the IEDs does narrow, however, montonically as the bias voltage increases. There is also evidence

of there being electrostatic waves that are launched into the plasma at higher biases by the impulsive, nearly step function change in substrate potential. This is particularly the case at higher voltages. These waves modulate the bulk plasma potential and are partly responsible for the modulation in the IED at energies below the peak.

4.3. Silicon and Silicon dioxide Etching

Most ion-assisted etching or deposition processes have thresholds or energy dependent reactions that are sensitive to the distribution of ion energies. Control over the IED therefore has important implications with respect to selectivity. For example, if the width of the IED can be made narrower than the difference in threshold energies of two materials, and can be positioned so as to discriminate between their threshold energies, the resulting selectivity could in principle be infinite. A broad IED as might be obtained by using a sinusoidal waveform may not allow for such discrimination.

Final predicted etch profiles for SiO_2 over Si are shown in Fig. 4.11 for a sin wave and tailored waveforms having α = 5% through 20%. The IEDs for these cases are shown in Fig. 4.5 and 4.7. Polymer formation is accelerated by low-energy ion bombardment whereas the etch process and polymer removal is initiated by high-energy ion bombardment. Polymer is necessary for chemical sputtering of SiO_2 in fluorocarbon plasmas as the carbon in the polymer aids in removal of oxygen in the SiO_2. Lack of polymer can actually reduce the etch rate even at high ion energies by removing the reaction precursor. Selectivity of etching SiO_2 over Si is enabled by the low rate of reaction of Si with the polymer, which results in there being a thicker polymer layer on Si. A thicker polymer layer impedes the delivery of activation energy to the polymer-Si (or SiO_2) interface, thereby slowing or stopping the etch. For the waveforms having

lower values of α, the ions are low enough in energy that the polymerization reactions dominate over etching, and an etch stop occurs. This happens deep into the trench as ion energies are degraded after reflection off of sidewalls. Upon increasing α, the ion energies increase and the angular distributions narrow. As a result, there is less polymerization and less side-wall scattering. The feature is cleared while the IEDs are able to discriminate well between the threshold energies of SiO_2 and Si. The end result is high selectivity.

The average etch depth across the feature as a function of time is shown in Fig. 4.12 for different values of α. The etch rates have been scaled to match the reported experimental etch rates obtained for a sinusoidal waveform with a peak-to-peak voltage of 200 V.[A] The aspect ratio dependent etching (ARDE) is severe for low values of α as indicated by the progressively lower etch rate (slope of the line) with depth leading in increasing amount of polymerization, eventually leading to an etch stop. This is also the case for the sinusoidal bias, that has a larger proportion of low energy ions. The etch rates increase with there being less ARDE as the positive portion of a cycle is increased (increasing α). The maximum etch rate is obtained with the α = 10% voltage waveform with there being good selectivity. However, as we approach the sinusoidal waveforms (α >10-20%) the etch rates begin to decrease again. As the IEDs broaden, the rate of polymerizing reactions increase and so the etch stop progresses more slowly.

Etch profiles at various times are shown in Fig. 4.13, for the tailored waveform (α = 10%) for peak-to-peak voltages of 200 V through 1500 V. Average etch depths as a function of time are shown in Fig. 4.14. As the peak-to-peak voltage is increased the ions have a higher energy on average and the etch proceeds more rapidly while there is less net polymer deposition. As a result the IEDs fail to discriminate between SiO_2 and Si at the higher biases and there is

considerable overetching into the underlying Si. Although the positioning of the peak of the IEDs allows for higher etch rates, the selectivity that is obtained is also lower.

4.4. Etching Recipes

Etching of features for microelectronics devices is often a multi-step process.[3-5] In addition to the initial steps that remove top layers such as antireflection coatings or native oxides (in the case of p-Si), etching of high aspect ratio (HAR) features usually consist of at least two steps. The first step is the main etch which is usually performed at high biases with non-polymerizing chemistries that produce a non-selective but rapid etch. The second step is the over-etch which is commenced when the interface is approached. This step is performed at lower biases and with a highly polymerizing chemistry that aids in selectivity. Traditionally, the steps are differentiated by controlling gas flow parameters such as gas mixture, flow rate, and pressure in addition to bias voltage. If this strategy is used, the change in gas composition in the reactor requires a finite period of time. Since gas transport is diffusive at low pressures, there will be components of both gas mixtures (main etch and over-etch) in the reactor at the same time. (See Figure 4.15a). The remnants of the main etch gases in the reactor during the over-etch step could compromise the ability to obtain high selectivity. As a result, one is motivated to develop recipes that rely only on the change in electrical characteristics which can be changed virtually instantaneously while using the same gas mixture for the main-etch and over-etch steps.

To accomplish these goals, we used the tailored bias voltage waveform and made use of the fact that the energy of the peak of the IEDs can be positioned by varying voltage amplitudes. The bias voltage as a function of time is conceptually shown in Fig. 4.15b. As the etch progresses from etch to over-etch, the bias voltage is either sharply or gradually reduced so that

the etch transitions from being rapid but non-selective to being selective but slower. If we regulate the peak of the IEDs to be such that it is able to distinguish between the thresholds of SiO_2 and Si then, in principle, infinite selectivity can be obtained while having a rapid etch.

Etch recipes were investigated for α = 10% waveforms where the main etch step is performed with a peak-to-peak potential of 1500 V and the over-etch step is performed with a lower voltage. The average etch depth across the feature as a function of time is shown in Fig. 4.16 for α = 10% when the voltage is changed at t = 4.5 s. The etch proceeds rapidly through the main etch step as polymerization is nominal (but adequate). In the absence of changing the voltage, the etch proceeds through the SiO_2-Si interface with poor selectivity. Upon lowering the peak-to-peak voltage at t = 4.5 s, the etch rate slows while the selectivity improves. The end result is that a recipe having a large peak-to-peak voltage followed by a lower voltage can achieve the same selectivity but with higher net rate than using only the more selective lower voltage. For example, the 1500 V-to-300 V recipe clears the feature with high selectivity in ≈12 s whereas using a 300 V waveform alone requires ≈20 s.

The average etch depth across the feature as a function of time is shown in Fig. 4.17a for main etch step of 1500 V (peak-to-peak, α = 10%) and an over-etch step of 200 V (peak-to-peak, α = 10%) while changing the voltage at different times. In this case, the IEDs are narrow for the over-etch step which discriminates well between the thresholds of SiO_2 and Si, and a highly selective etch is obtained, irrespective of the time of change of voltage. Similar results are shown in Fig. 4.17b for an over-etch voltage of 500 V. High selectivity and high rates can be obtained judicious choices of the main-etch and over-etch voltages, and the value of α. The nearly instantaneous change of etch rate afforded by the tailored bias enables precision control of the process. Timing the transition to the lower voltage to be as late as possible gains in rate

while risking undesirable over-etch at other locations on the wafer due to variations in the magnitude of the ion fluxes.

The profiles for a tailored waveform having α = 10%, 1500 V (peak-to-peak) main etch and an over-etch of 200 V (peak-to-peak) are shown in Fig. 4.18. The main etch step is run for 5 s and the over-etch lasts for 22.5 s. The time at which the voltage is changed from 1500 V to 200 V is determined by the lowest point of the taper. Had these conditions produced a flatter bottom to the trench, the main etch would have been able to proceed to a lower average depth prior to switching to the lower voltage. Small adjustments in the value of the α recoups some flatness of the profile bottom, and so enables the main etch to proceed closer to the interface before changing to the lower voltage.

4.5. Conclusions

The influence of the shape of the rf bias voltage waveform on ion energy distributions incident onto the wafer has been discussed based on results from a computational investigation using a reactor scale model coupled to a feature profile model. A non-sinusoidal waveform consisting of a quasi-dc negative bias with a narrow positive excursion was investigated in the context of fluorocarbon plasma etching of SiO_2 and Si. The tailored bias voltage waveform allows for precise control over the shape of the IED and the resulting distributions are less sensitive to the mass of the ions than the sinusoidal waveforms. The method for controlling the shape of the IED has potential for improving control of critical dimensions of etched features. The potential was demonstrated by proposing etching recipes based on reapidly changing the shape of the IED from one providing for a rapid but non-selective etch to one providing a slower but selective process.

4.6 Figures

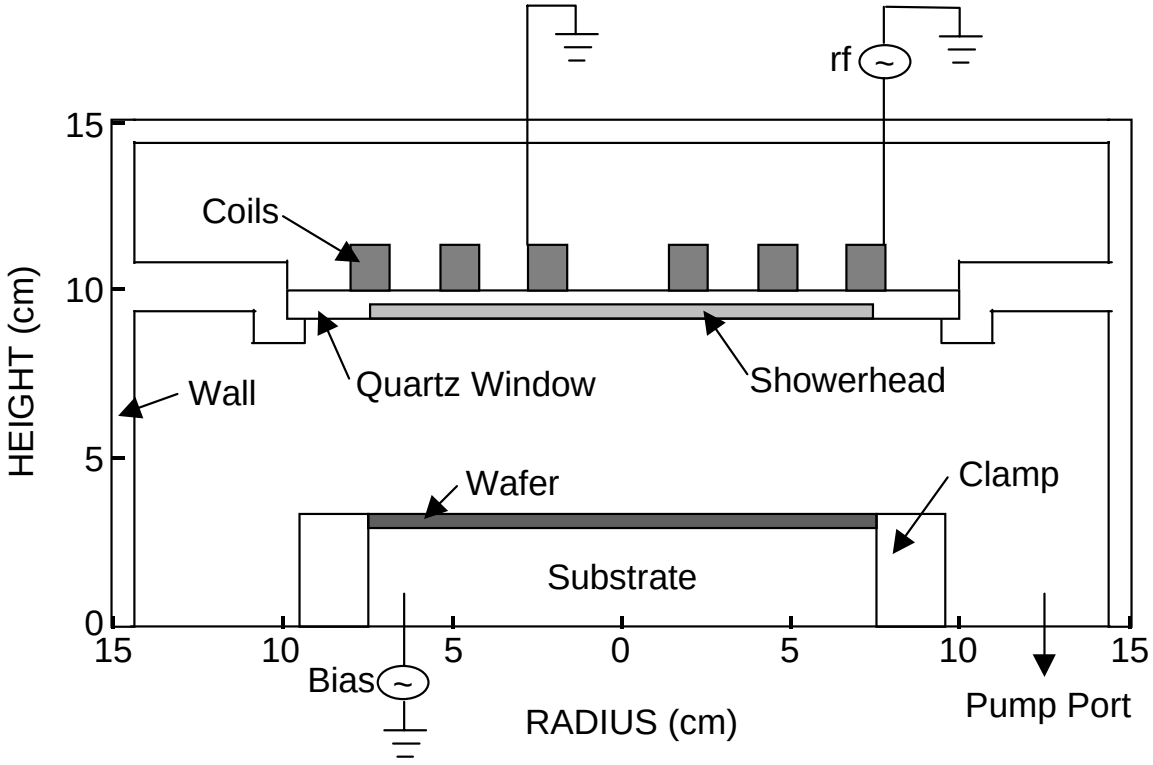

Fig. 4.1. Schematic of the model ICP reactor that was used in all the simulations

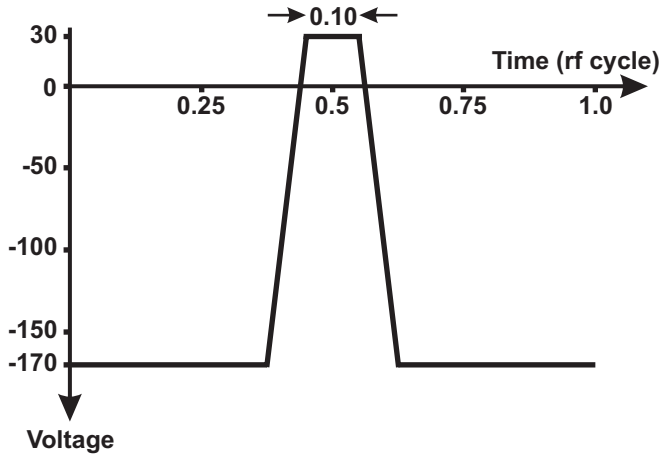

Fig. 4.2: Schematic of the tailored voltage bias waveform. The voltage form represented is the "10% waveform" based on the percent of cycle with constant positive voltage.

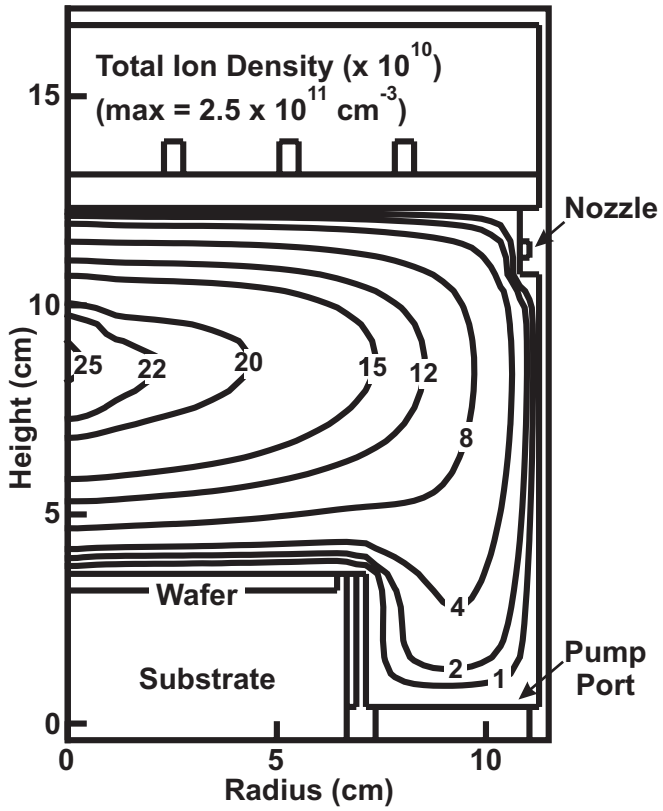

Fig. 4.3: Total Ion Density for the base case (Ar/C_4F_8, 500 W ICP Power, 15 mTorr, 100 sccm) and 200 V (peak-to-peak) substrate voltage. Contour levels shown are on a scale of 10^{10}

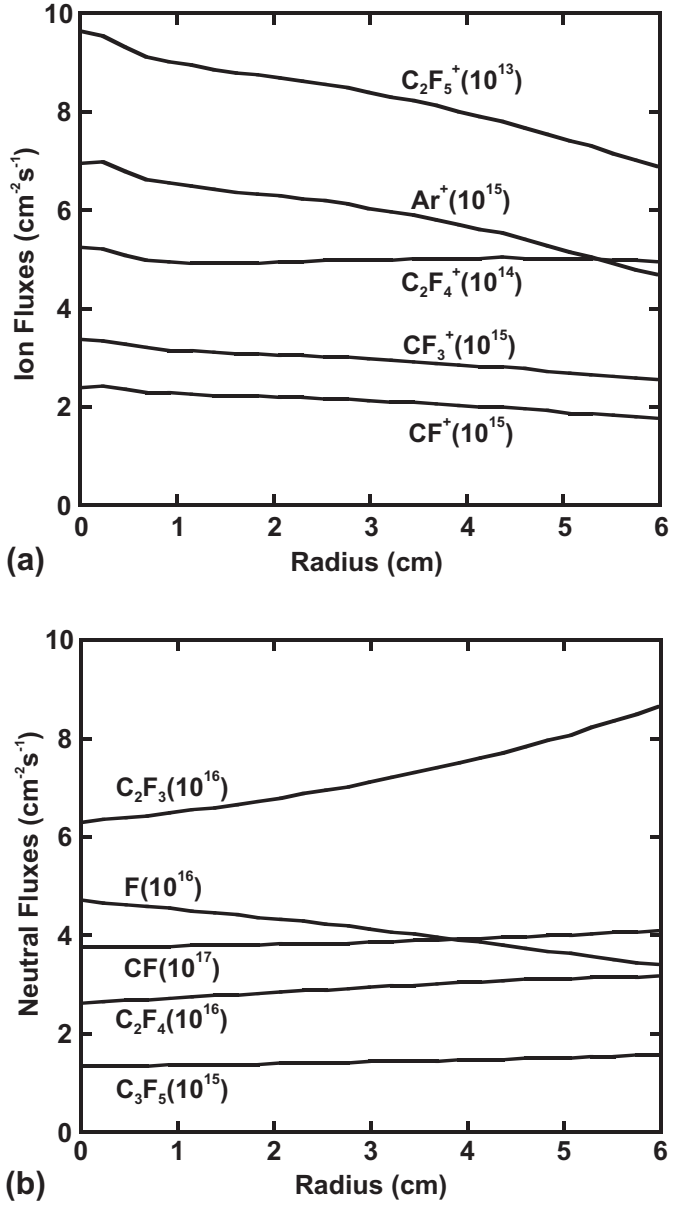

Fig. 4.4: Fluxes to the surface as a function of radius for the base case conditions for Ar/C_4F_8 plasma. CF, C_2F_3, and F are the dominant neutral radicals. Ar^+, CF_3^+, and CF^+ are the dominant ions.

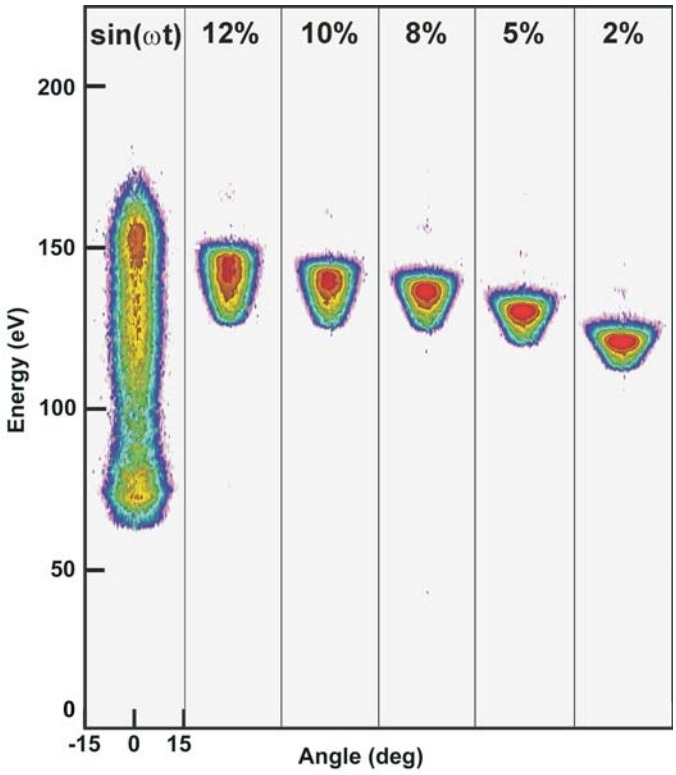

Fig. 4.5: Total ion energy and angular distributions, averaged over the wafer, for different bias voltage waveforms. The tailored voltage waveform significantly narrows the ion energy spread.

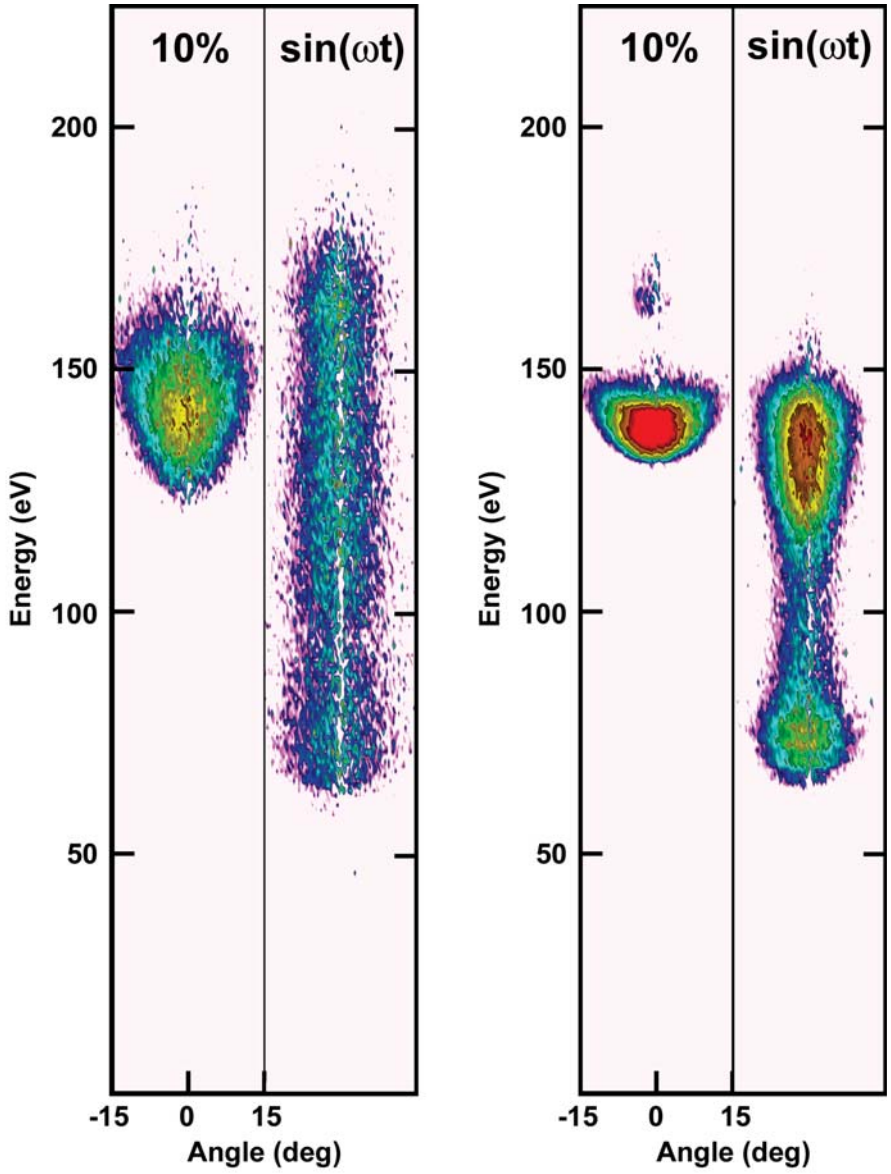

Fig. 4.6: Energy and angular distributions for F^+ (left) and $C_4F_7^+$ (right) ions, for a = 10% waveform and sinusoidal waveform. The tailored voltage waveform affects both the low and high mass ions in the same manner.

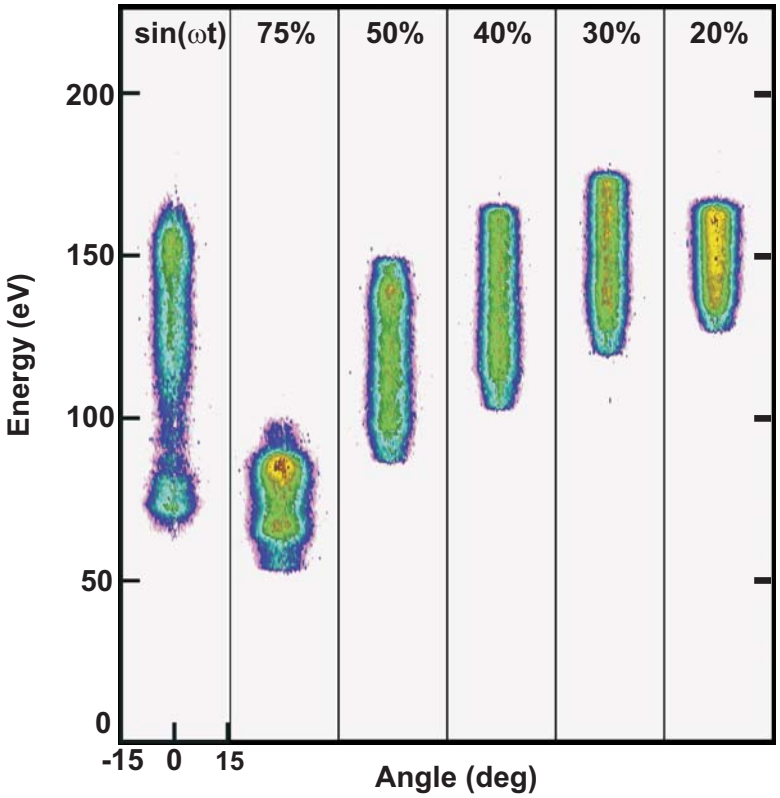

Fig. 4.7: Total ion energy and angular distributions, averaged over the wafer, for different bias voltage waveforms. The IEDs attain forms similar to that of sinusoidal IED on increasing duration of positive voltage.

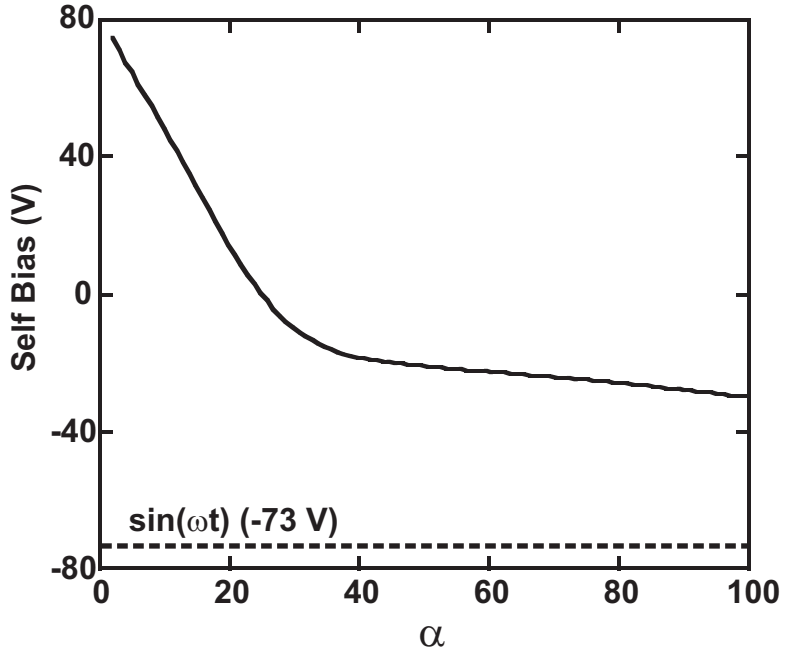

Fig. 4.8: Relation between the self-generated dc bias and a. The self-generated dc bias voltage is -73 V for the sinusoidal waveform at base case conditions.

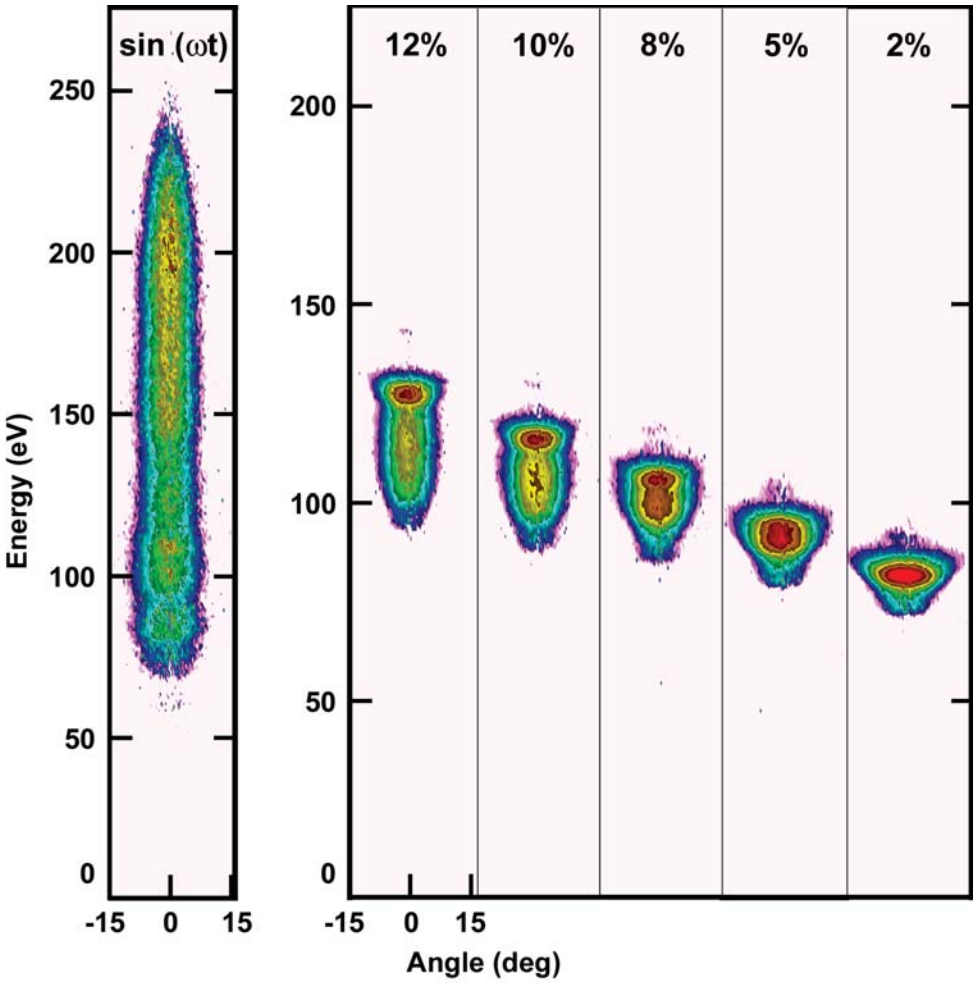

Fig. 4.9: Total ion energy and angular distributions, averaged over the wafer, for different bias voltage waveforms at a frequency of 2 MHz. The tailored voltage waveform can use increasing frequency as an alternate route to narrow IED.

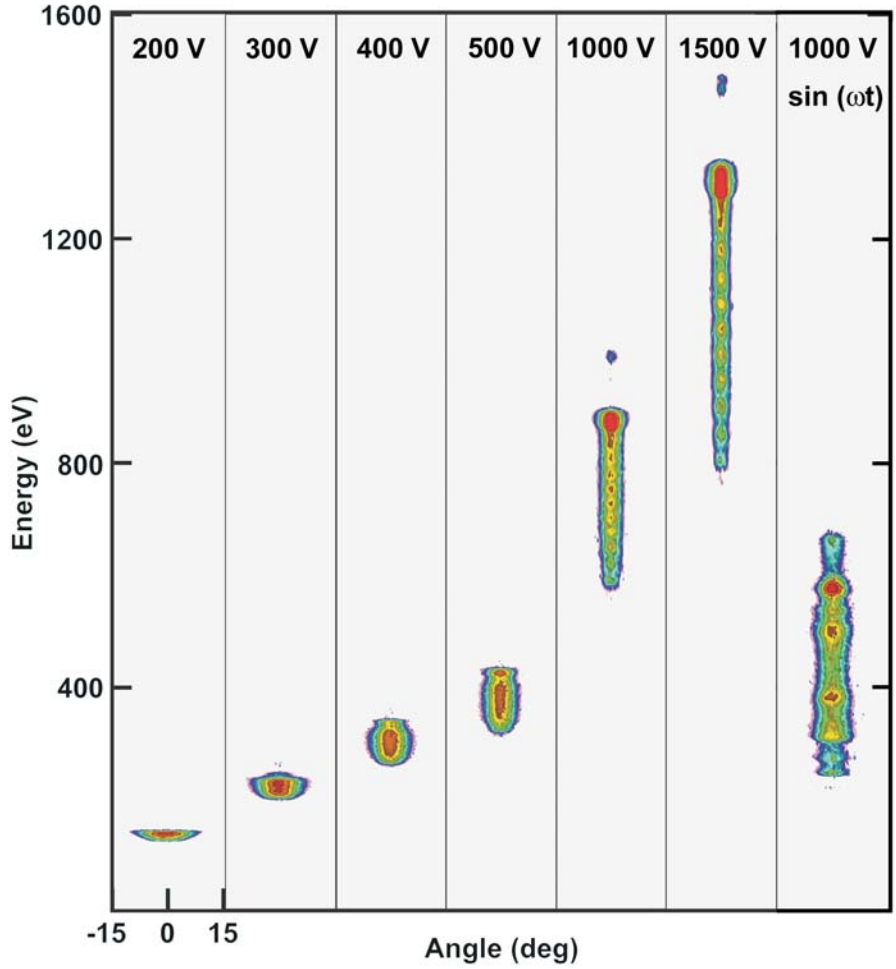

Fig. 4.10: Total ion energy and angular distributions, averaged over the wafer, for different peak-to-peak voltages corresponding to the 10% waveform. The change in voltage amplitudes allows peak positioning of the IEDs.

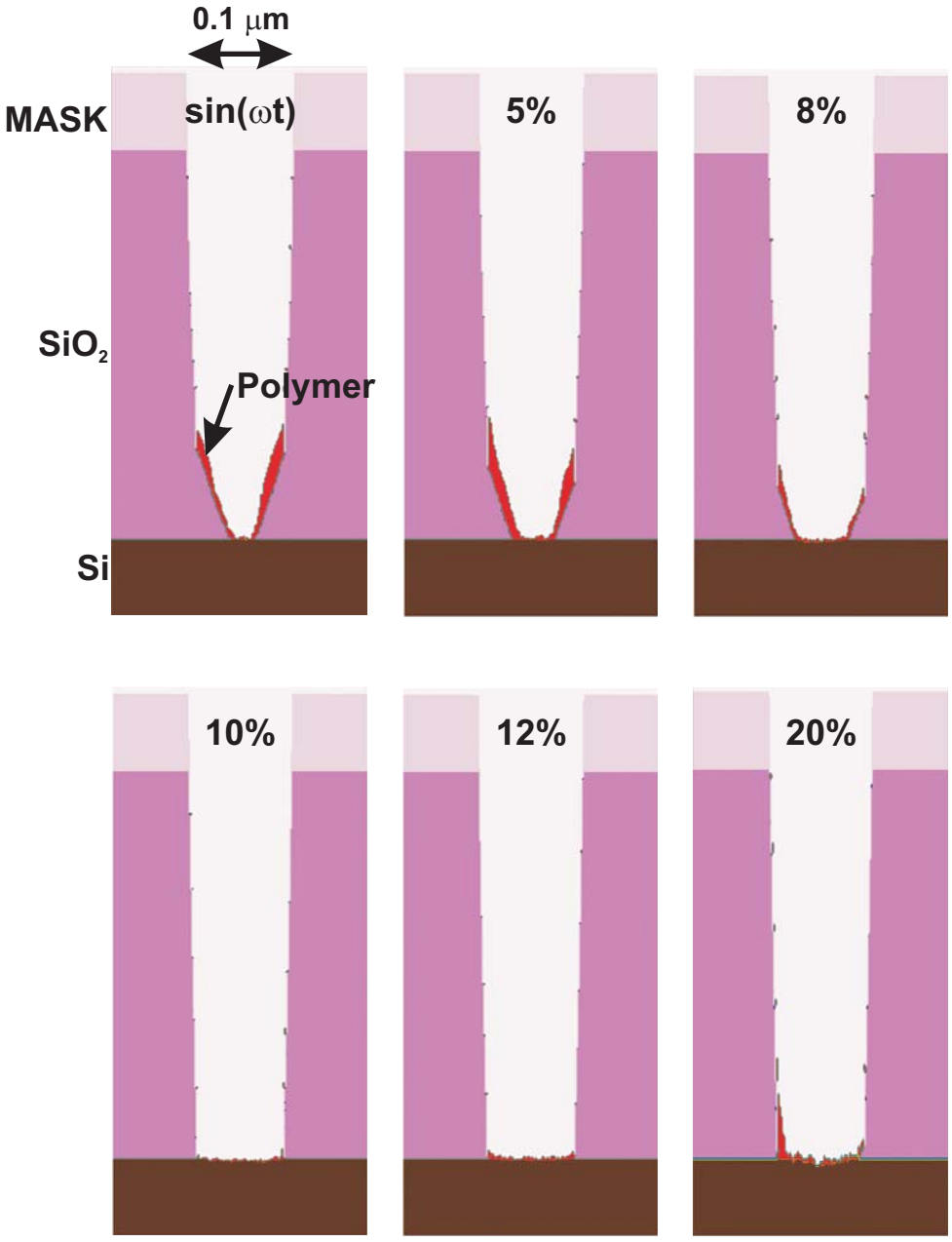

Fig. 4.11: Final etch profiles for different voltage bias waveforms. X% indicates percent of cycle with constant positive voltage. Low X% produces IEDs which result in etch-stop layers.

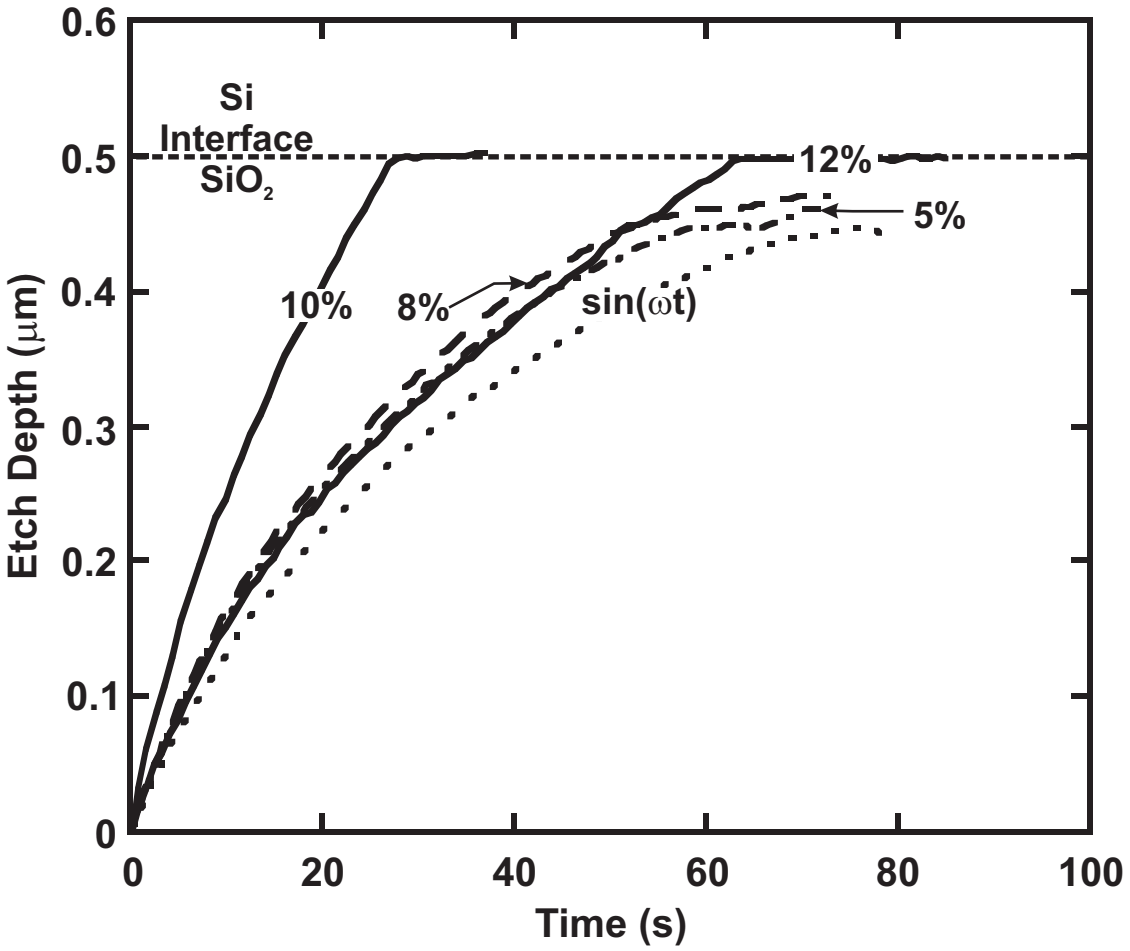

Fig. 4.12: Etch Depth as a function of time. The etch rate increases as the percent of cycle with constant positive voltage is increased for the tailored voltage bias. Highest etch rate is obtained for the 10% voltage waveform.

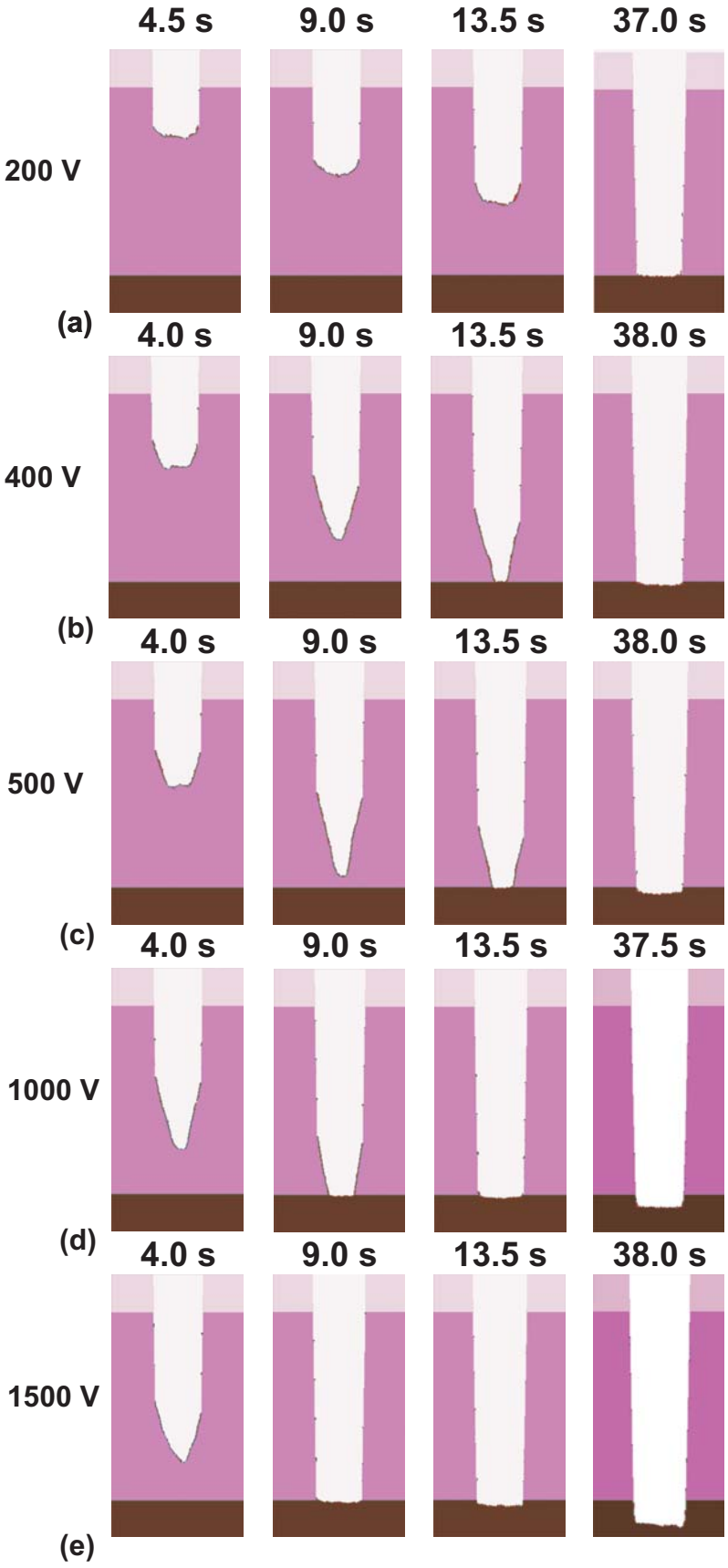

Fig. 4.13: Etch profiles at various times for different peak-to-peak voltages using 10% waveform (a) 200 V (b) 400 V (c) 500 V (d) 1000 V (e) 1500 V

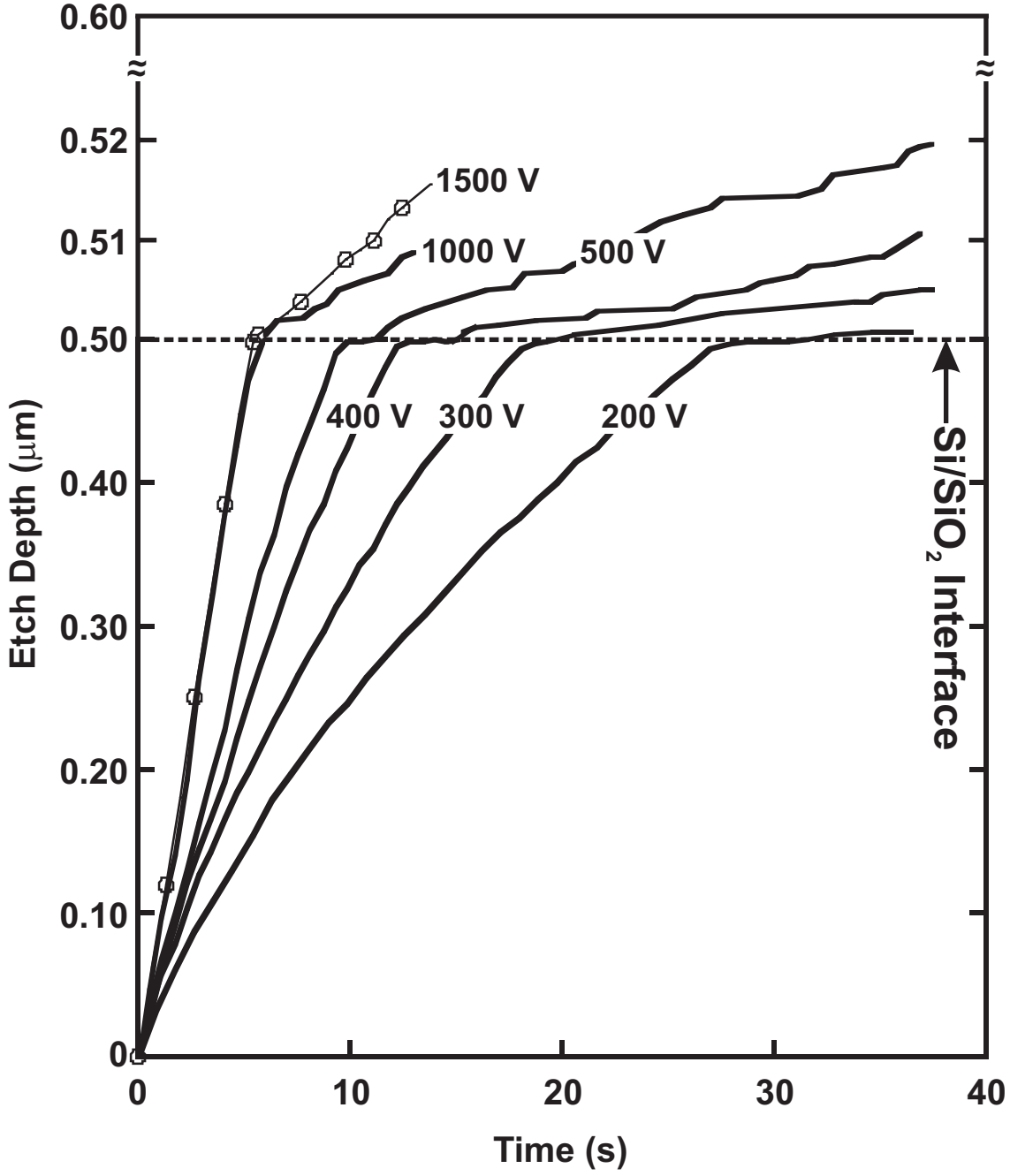

Fig. 4.14: Etch Depth as a function of time for different peak-to-peak voltages for the 10% waveform. The etch rate increases as the voltage is increased but the selectivity decreases.

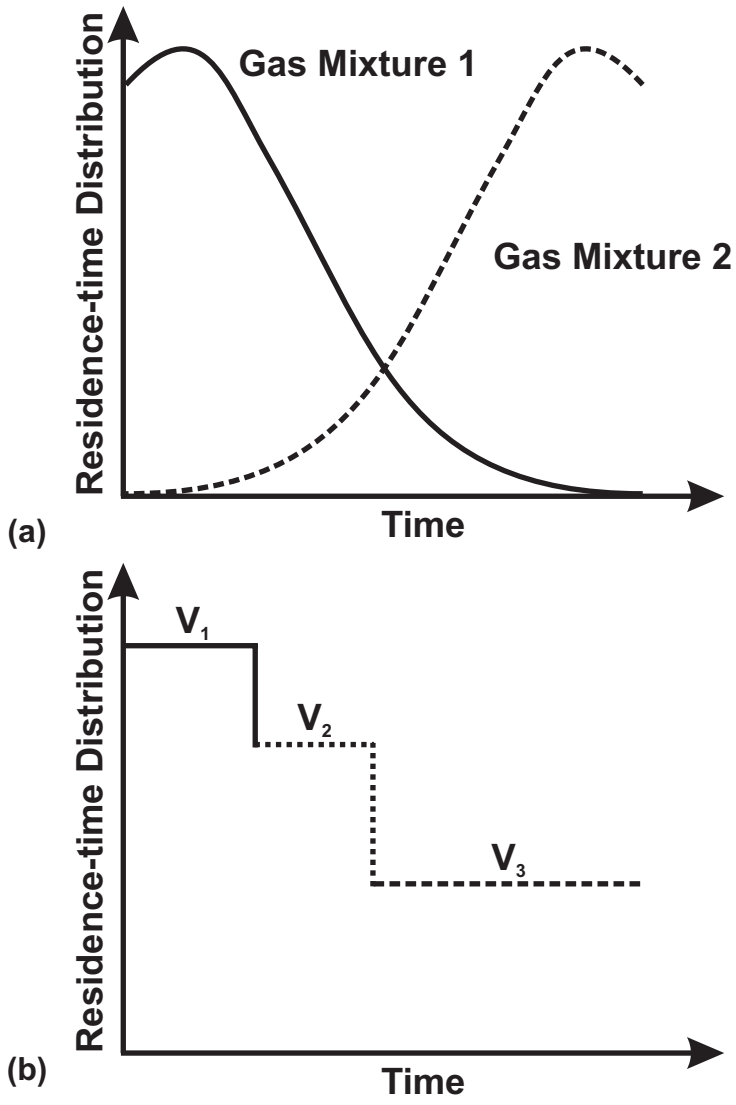

Fig. 4.15: Residence time distribution functions (a) Gas flowing through a reactor (b) Voltage amplitude change. Non-gaussian distributions for the voltage gives better control during an etch process.

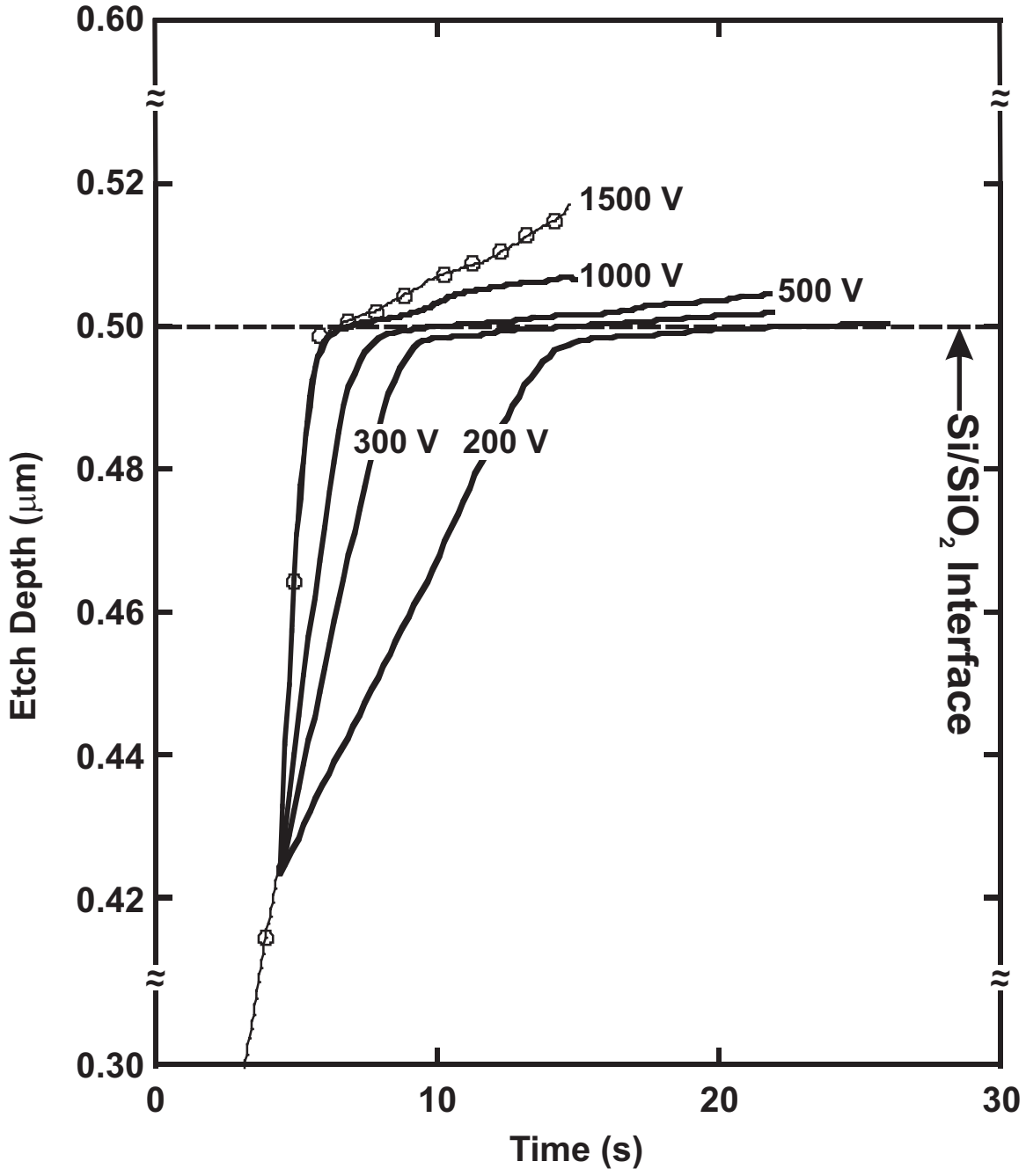

Fig. 4.16: Etch Depth as a function of time for different peak-to-peak voltages for the 10% waveform, corresponding to the etching recipes. The voltage amplitude is changed midway from 1500 V to different voltages for the over-etch step, keeping time of change of voltage fixed.

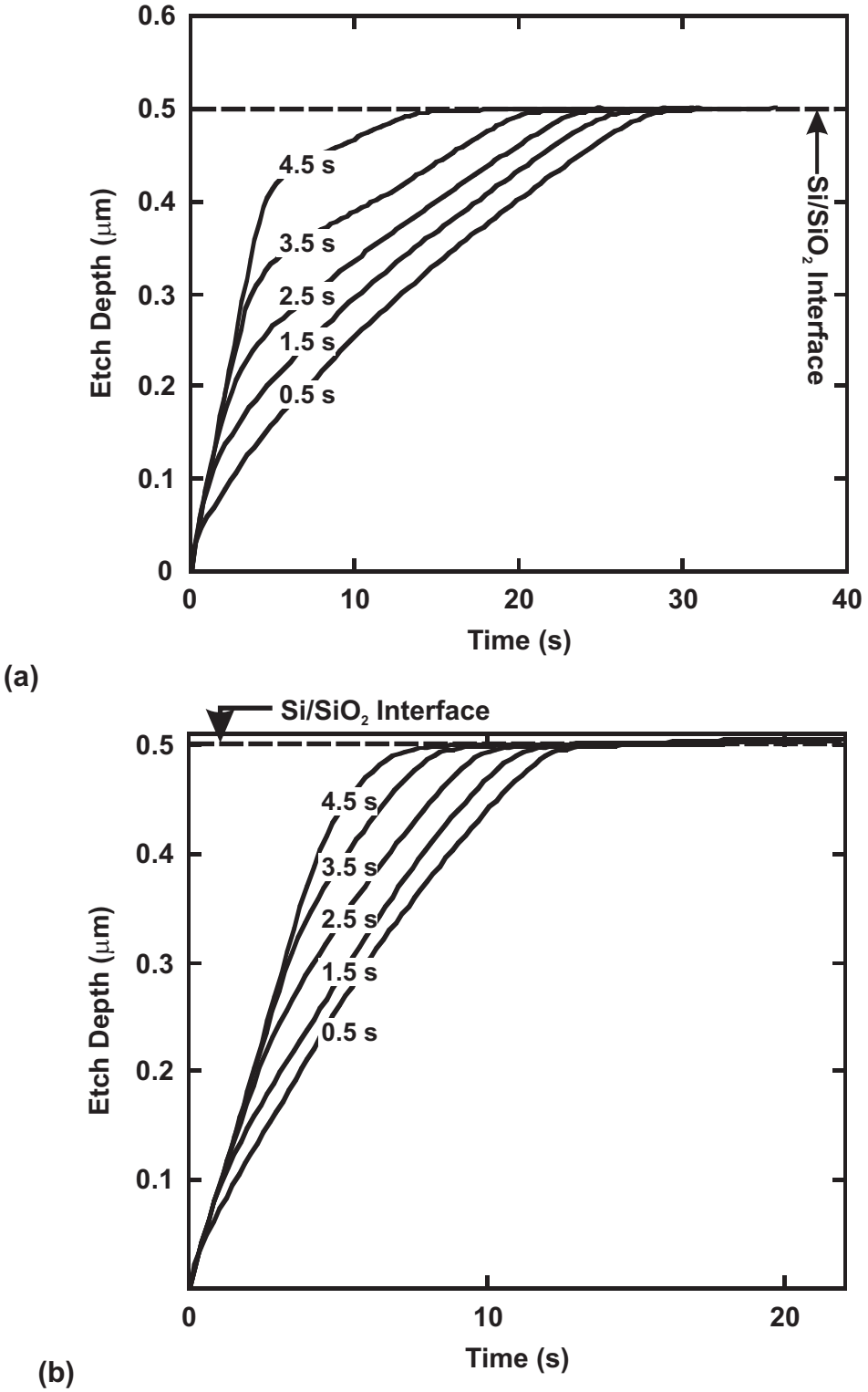

Fig. 4.17: (a) Etch Depth as a function of time corresponding to etching recipe which uses a main-etch step of 1500 V and an over-etch step of 200 V. The times of change of voltages is varied.

(b) Etch Depth as a function of time corresponding to etching recipe which uses a main-etch step of 1500 V and an over-etch step of 500 V. The times of change of voltages is varied.

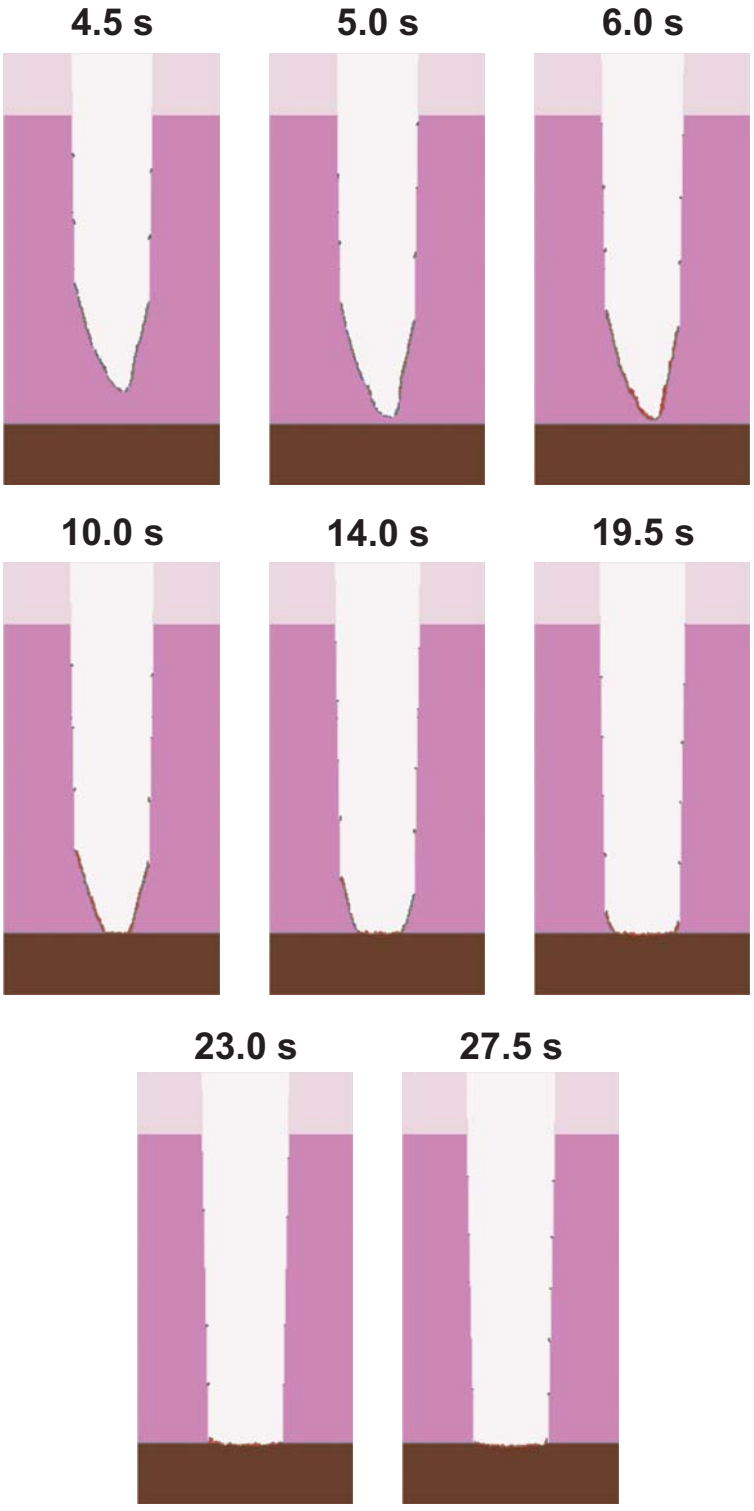

Fig. 4.18: Etching recipe with single voltage amplitude change from 1500 V (5 s) to 200 V (22.5 s).

4.7 References

[1] X. Li, L. Ling, X. Hua, G. S. Oehrlein, Y. Wang, A. V. Vasenkov and M. J. Kushner, J. Vac. Sci. Technol. **22**, 500 (2004)

[2] S.-B. Wang and A.E. Wendt, J. Vac. Sci. Technol. **19**, 2425 (2001)

[3] C. Monget, D. Fuard, O. Joubert, and J.P. Panabiere, Microelectron. Eng. **46**, 349 (1999)

[4] M.-R. Lin, P. Fang, F. Heiler, R. Rakkhit and L. Shen, IEEE Electron Device Lett. **15**, 25 (1994)

[5] H.-C. Cheng, W. Lin, T.-K. Kang, Y.-C. Perng and B.-T. Dai, IEEE Electron Device Lett. **19**, 183 (1998)

5. CONCLUSIONS

5.1 Conclusions

Ion energy distributions (IEDs) are one of the primary factors governing the etching or deposition characteristics in plasma-aided microelectronics manufacturing processes. Being important parameters, IEDs and angular distributions have been the subject of several experimental and computational investigations in high-density plasmas. The energy provided to the substrate surface upon ion impact can enhance chemical reactions via several mechanisms, demonstrated in simulation and ion beam experiments. Control of ion energies is typically obtained by varying the amplitude or frequency of a radio frequency (rf) sinusoidal bias voltage applied to the substrate. The resulting ion energy is, however, generally broad. Control of the ion energy distribution was computationally investigated by applying a tailored non-sinusoidal bias waveform to the substrate of an inductively coupled plasma. The tailored waveform can be implemented in different conditions (rf and dc) resulting in different plasma characteristics and entirely different processes.

In a scenario involving an rf bias, the tailored voltage waveform, a quasi negative bias having a short positive pulse each cycle, produced a narrow IED whose width was controllable based on the length of the positive spike and frequency. The tailored bias voltage waveform allows for greater control over the IED obtained and is insensitive to the mass of ions. Controlling the width and shaped of the IED can help improve etch selectivity by distinguishing between threshold energies of surface processes. Thus, selectivity between Si and SiO_2 in fluorocarbon plasmas was thus controlled by adjusting the width and energy of the IED. The narrow IED results in a high selectivity and at faster etching rates. The control over the IED

demonstrated was further extended to the concept of developing etching recipes. Traditionally, the gas mixture was changed to obtain the selectivity. Etching recipes were developed by changing only the voltage amplitude of the tailored bias voltage waveform without changing the gas mixture. These etching recipes demonstrate highly selective etch profiles at high etch rates can be obtained without change of gas mixture.

APPENDIX A: SURFACE REACTION MECHANISM

Surface reaction mechanism for fluorocarbon etching[1] of porous and nonporous SiO_2 used in the present study is given below:

Species and symbols definition:

CF_3^+ represents all ions,

CF_x and C_xF_y radicals represent polymerizing species.

Species	Symbol
Fluorocarbon polymer	P
Hydrogenated polymer	HP
Activated Species	*
Ions	+
Gas phase species	g
Hot neutrals	h
Surface species	s

Surface reaction mechanism

Reaction[a,b]	Probability	Footnote
Formation of complex at polymer-SiO_2 interface:	p_0	
$SiO_{2s} + CF_{xg} \rightarrow SiO_2CF_{xs}$	0.1	
$SiO_{2s} + C_xF_{yg} \rightarrow SiO_2C_xF_{ys}$	0.1	
Low energy Ion activation to form polymer and activated complex site	p_0	
$SiO_2CF_s + CF_{3g}^+ \rightarrow SiO_2CF_s^* + CF_{3h}$	0.1	c
$SiO_2CF_{2s} + CF_{3g}^+ \rightarrow SiO_2CF_{2s}^* + CF_{3h}$	0.1	c
$SiO_2C_2F_{3s} + CF_{3g}^+ \rightarrow SiO_2C_2F_{3s}^* + CF_{3h}$	0.1	c
$SiO_2C_2F_{4s} + CF_{3g}^+ \rightarrow SiO_2C_2F_{4s}^* + CF_{3h}$	0.1	c
$SiO_2CF_s + CF_{3g}^+ \rightarrow SiO_2CF_s + P_s$	0.1	c
$SiO_2CF_{2s} + CF_{3g}^+ \rightarrow SiO_2CF_{2s} + P_s$	0.1	c
$SiO_2C_2F_{3s} + CF_{3g}^+ \rightarrow SiO_2C_2F_{3s} + P_s$	0.1	c
$SiO_2C_2F_{4s} + CF_{3g}^+ \rightarrow SiO_2C_2F_{4s} + P_s$	0.1	c
Ion activated dissociation of complex (CF_3^+)[d]	p_0	

$SiO_2CF_s + CF_{3g}^+ \rightarrow SiO_{2s} + CF_g + CF_{3h}$	0.08	d
$SiO_2CF_{2s} + CF_{3g}^+ \rightarrow SiO_{2s} + CF_{2g} + CF_{3h}$	0.08	d
$SiO_2C_2F_{3s} + CF_{3g}^+ \rightarrow SiOCF_{3s} + CO_g + CF_{3h}$	0.90	d
$SiO_2C_2F_{3s} + CF_{3g}^+ \rightarrow SiO_{2s} + C_2F_{3g} + CF_{3h}$	0.03	d
$SiO_2C_2F_{4s} + CF_{3g}^+ \rightarrow SiOCF_{4s} + CO_g + CF_{3h}$	0.90	d
$SiO_2C_2F_{4s} + CF_{3g}^+ \rightarrow SiO_{2s} + C_2F_{4g} + CF_{3h}$	0.03	d
$SiOCF_{3s} + CF_{3g}^+ \rightarrow SiF_{2s} + COF_g + CF_{3h}$	0.01	d
$SiOCF_{4s} + CF_{3g}^+ \rightarrow SiF_{3s} + COF_g + CF_{3h}$	0.01	d
$SiO_2CF_s^* + CF_{3g}^+ \rightarrow SiO_{2s} + CF_g + CF_{3h}$	0.08	d
$SiO_2CF_{2s}^* + CF_{3g}^+ \rightarrow SiO_{2s} + CF_{2g} + CF_{3h}$	0.08	d
$SiO_2C_2F_{3s}^* + CF_{3g}^+ \rightarrow SiOCF_{3s} + CO_g + CF_{3h}$	0.90	d
$SiO_2C_2F_{3s}^* + CF_{3g}^+ \rightarrow SiO_{2s} + C_2F_{3g} + CF_{3h}$	0.03	d
$SiO_2C_2F_{4s}^* + CF_{3g}^+ \rightarrow SiOCF_{4s} + CO_g + CF_{3h}$	0.90	d
$SiO_2C_2F_{4s}^* + CF_{3g}^+ \rightarrow SiO_{2s} + C_2F_{4g} + CF_{3h}$	0.03	d
$SiOCF_{3s}^* + CF_{3g}^+ \rightarrow SiF_{2s} + COF_g + CF_{3h}$	0.01	d
$SiOCF_{4s}^* + CF_{3g}^+ \rightarrow SiF_{3s} + COF_g + CF_{3h}$	0.01	d
$SiF_{3s}^* + CF_{3g}^+ \rightarrow SiF_{3g} + CF_{3h}$	0.99	d
Reactions with polymerizing specie (CF_x, C_xF_y)	p_0	
$SiO_2CF_s + CF_{xg} \rightarrow SiO_2C_2F_{3s}$	0.10	
$SiO_2CF_{2s} + CF_{xg} \rightarrow SiO_2C_2F_{4s}$	0.10	
$SiO_2CF_s^* + CF_{xg} \rightarrow SiO_2CF_s + P_s$	0.5	
$SiO_2CF_{2s}^* + CF_{xg} \rightarrow SiO_2CF_{2s} + P_s$	0.5	
$SiO_2C_2F_{3s}^* + CF_{xg} \rightarrow SiO_2C_2F_{3s} + P_s$	0.5	
$SiO_2C_2F_{4s}^* + CF_{xg} \rightarrow SiO_2C_2F_{4s} + P_s$	0.5	
$SiO_2CF_s^* + C_xF_{yg} \rightarrow SiO_2CF_s + P_s$	0.5	
$SiO_2CF_{2s}^* + C_xF_{yg} \rightarrow SiO_2CF_{2s} + P_s$	0.5	
$SiO_2C_2F_{3s}^* + C_xF_{yg} \rightarrow SiO_2C_2F_{3s} + P_s$	0.5	
$SiO_2C_2F_{4s}^* + C_xF_{yg} \rightarrow SiO_2C_2F_{4s} + P_s$	0.5	
$Si_s + CF_{xg} \rightarrow Si_s + P_s$	0.15	
$Si_s + C_xF_{yg} \rightarrow Si_s + P_s$	0.15	
$SiF_s + CF_{xg} \rightarrow SiF_s + P_s$	0.15	
$SiF_{2s} + CF_{xg} \rightarrow SiF_{2s} + P_s$	0.15	
$SiF_s + C_xF_{yg} \rightarrow SiF_s + P_s$	0.15	
$SiF_{2s} + C_xF_{yg} \rightarrow SiF_{2s} + P_s$	0.15	
$SiF_{3s} + CF_{xg} \rightarrow SiF_{3s} + P_s$	0.15	
$SiF_{3s} + C_xF_{yg} \rightarrow SiF_{3s} + P_s$	0.15	
Fluorination reactions		
$Si_s + F_g \rightarrow SiF_s$	0.05	
$SiF_s + F_g \rightarrow SiF_{2s}$	0.05	

$SiF_{2s} + F_g \rightarrow SiF_{3s}$	0.05	
$SiF_{3s} + F_g \rightarrow SiF_{4g}$	0.10	
$SiO_2CF_s + F_g \rightarrow SiF_{2s} + CO_{2g}$	0.01	
$SiO_2CF_{2s} + F_g \rightarrow SiF_{3s} + CO_{2g}$	0.01	
Reactions on polymer surface		
$P_s + F_g \rightarrow CF_{2g}$	0.03	
$P_s + H_g \rightarrow P_s + HP_s$	0.90	
$P_s + C_xF_{yg} \rightarrow P_s + P_s$	0.15	
$P_s + CF_{xg} \rightarrow P_s + P_s$	0.15	
$P_s + CF_{3g}^+ \rightarrow CF_{3h} + CF_{2g}$	0.15	d
$HP_s + F_g \rightarrow CF_{2g}$	0.03	f
$HP_s + H_g \rightarrow HP_s + HP_s$	0.99	f
$HP_s + C_xF_{yg} \rightarrow HP_s + HP_s$	0.05	f
$HP_s + CF_{xg} \rightarrow HP_s + HP_s$	0.05	f
$HP_s + CF_{3g}^+ \rightarrow CF_{3h} + CF_{2g}$	0.28	e,f

[a] All ions return as a hot neutral. Ions and hot neutrals have the same mechanism.

[b] In reactions with no change chemically, the gas species are reflected of the surface.

[c] $p(E_i) = p_0 \times \max\left(0, 1 - \frac{E_i}{E_c}\right)$, E_c = 70 eV. E_c refers to maximum allowable energy (in eV) and p_o is the probability at 0 eV.

[d] $p(\theta) = p_0 \left[\frac{E^n - E_{th}^n}{E_r^n - E_{th}^n}\right] f(\theta)$, E_{th} = 70 eV, E_r = 140 eV and n = 0.97. E_{th} refers to threshold energy, E_r refers to reference energy, (both energies in eV) and p_o is the probability at E_r.

[e] $p(\theta) = p_0 \left[\frac{E^n - E_{th}^n}{E_r^n - E_{th}^n}\right] f(\theta)$, E_{th} = 125 eV, E_r = 175 eV and n = 0.98.

[f] Reactions on P and HP surfaces are similar with different probabilities.

[1] A. Sankaran and M. J. Kushner, J. Vac. Sci. Technol. A **22**, 1242 (2004)

APPENDIX B: LIST OF REACTIONS OF Ar/C_4F_8

The reaction chemistry[20] for an Ar/C_4F_8 gas mixture used in the present study is given below:

Reaction[a]	Rate Coefficient[b]	Reference
$e + Ar \rightarrow Ar + e$	c	1
$e + Ar \rightarrow Ar^{*} + e$	c	2
$e + Ar \rightarrow Ar^{**} + e$	c	2
$e + Ar \rightarrow Ar^{+} + e + e$	c	3
$e + Ar^{*} \rightarrow Ar^{+} + e + e$	c	4
$e + Ar^{*} \rightarrow Ar + e$	c	2[d]
$e + Ar^{*} \rightarrow Ar^{**} + e$	c	5
$e + Ar^{**} \rightarrow Ar + e$	c	2[d]
$e + Ar^{**} \rightarrow Ar^{+} + e + e$	c	6
$e + Ar^{**} \rightarrow Ar^{*} + e$	c	5[d]
$e + F \rightarrow F + e$	c	7
$e + F \rightarrow F\ (ex) + e$	c	7
$e + F \rightarrow F^{+} + e + e$	c	7
$e + F_2 \rightarrow F_2 + e$	c	8
$e + F_2 \rightarrow F_2\ (v) + e$	c	8
$e + F_2 \rightarrow F_2\ (ex) + e$	c	8
$e + F_2 \rightarrow F_2 + e$	c	8
$e + F_2 \rightarrow F^{+} + F^{-}$	c	8

$e + F_2 \rightarrow F_2^+ + e + e$	c	8
$e + CF \rightarrow CF + e$	c	9[e]
$e + CF \rightarrow CF\ (v) + e$	c	9[e]
$e + CF \rightarrow c + F + e$	c	9[e]
$e + CF \rightarrow CF^+ + e + e$	c	10
$e + CF_2 \rightarrow CF_2 + e$	c	11[f]
$e + CF_2 \rightarrow CF_2\ (v) + e$	c	11[f]
$e + CF_2 \rightarrow CF + F^-$	c	11[f]
$e + CF_2 \rightarrow CF + F + e$	c	11[f]
$e + CF_2 \rightarrow CF_2^+ + F + e + e$	c	12
$e + CF_2 \rightarrow CF^+ + F + e + e$	c	12
$e + CF_3 \rightarrow CF_3 + e$	c	11[f]
$e + CF_3 \rightarrow CF_3\ (v) + e$	c	11[f]
$e + CF_3 \rightarrow CF_2 + F + e$	c	11[f]
$e + CF_3 \rightarrow CF_3^+ + e + e$	c	12
$e + CF_3 \rightarrow CF_2^+ + F + e + e$	c	12
$e + CF_3 \rightarrow CF_2 + F^-$	c	11[f]
$e + CF_4 \rightarrow CF_4 + e$	c	11
$e + CF_4 \rightarrow CF_4\ (v) + e$	c	11
$e + CF_4 \rightarrow CF_3 + F^-$	c	11
$e + CF_4 \rightarrow CF_3^- + F$	c	11
$e + CF_4 \rightarrow CF_3 + F + e$	c	11

$e + CF_4 \rightarrow CF_3^+ + F + e + e$	c	11
$e + CF_4 \rightarrow CF_2 + F + F + e$	c	11
$e + CF_4 \rightarrow CF_3^+ + F^- + e$	c	11
$e + CF_4 \rightarrow CF + F + F_2 + e$	c	11
$e + C_2F_3 \rightarrow CF + CF_2 + e$	$1\times10^{-8}T_e^{0.91}\exp(-5.0/T_e)$	13[g]
$e + C_2F_4 \rightarrow C_2F_4 + e$	c	14, 15
$e + C_2F_4 \rightarrow C_2F_4\,(v) + e$	c	14, 15
$e + C_2F_4 \rightarrow CF_2 + CF_2 + e$	c	14, 15
$e + C_2F_4 \rightarrow C_2F_4^+ + e + e$	c	14, 15
$e + C_2F_4 \rightarrow C_2F_3^+ + F + e$	c	14, 15
$e + C_2F_4 \rightarrow CF^+ + CF_3^+ + e$	c	14, 15
$e + C_2F_5 \rightarrow C_2F_5 + e$	c	16[h]
$e + C_2F_5 \rightarrow C_2F_5\,(v) + e$	c	16[h]
$e + C_2F_5 \rightarrow CF_3^- + CF_2$	c	16[h]
$e + C_2F_5 \rightarrow CF_3 + CF_2 + e$	c	16[h]
$e + C_2F_5 \rightarrow CF_3^- + CF_2 + e + e$	c	17
$e + C_2F_5 \rightarrow C_2F_5^+ + e + e$	c	17
$e + C_2F_6 \rightarrow CF_3^+ + CF_3 + e + e$	c	16
$e + C_2F_6 \rightarrow C_2F_6 + e$	c	16
$e + C_2F_6 \rightarrow C_2F_6\,(v) + e$	c	16
$e + C_2F_6 \rightarrow CF_3 + CF_3^-$	c	16
$e + C_2F_6 \rightarrow C_2F_5 + F^-$	c	16

$e + C_2F_6 \rightarrow CF_3 + CF_3 + e$	c	16
$e + C_3F_5 \rightarrow C_2F_3 + CF_2 + e$	$1.8\times10^{-8}T_e^{0.52}\exp(-12.3/T_e)$	14, 15[g,i]
$e + C_3F_5 \rightarrow C_2F_4 + CF + e$	$1.8\times10^{-8}T_e^{0.52}\exp(-12.3/T_e)$	14, 15[g,i]
$e + C_3F_6 \rightarrow C_2F_6^+ + e$	$1.4\times10^{-8}T_e^{0.68}\exp(-10.6/T_e)$	14, 15[g,i]
$e + C_3F_6 \rightarrow C_2F_3 + CF_3 + e$	$1.8\times10^{-8}T_e^{0.52}\exp(-12.3/T_e)$	14, 15[g,i]
$e + C_3F_6 \rightarrow C_2F_4 + CF_2 + e$	$1.8\times10^{-8}T_e^{0.52}\exp(-12.3/T_e)$	14, 15[g,i]
$e + C_3F_7 \rightarrow C_2F_4 + CF_3 + e$	$1.8\times10^{-8}T_e^{0.52}\exp(-12.3/T_e)$	14, 15[g,i]
$e + C_4F_7 \rightarrow C_2F_4 + C_2F_3 + e$	$5.7\times10^{-8}T_e^{0.28}\exp(-8.0/T_e)$	16[g,h]
$e + C_4F_7 \rightarrow C_4F_7^+ + e + e$	$1.4\times10^{-8}T_e^{0.68}\exp(-10.6/T_e)$	16[g,h]
$e + C_4F_8 \rightarrow C_4F_8 + e$	c	18
$e + C_4F_8 \rightarrow C_4F_8\ (v) + e$	c	18
$e + C_4F_8 \rightarrow C_2F_4 + C_2F_4 + e$	c	18
$e + C_4F_8 \rightarrow C_4F_8^{-*}$	c	18
$e + C_4F_8 \rightarrow F^- + C_4F_7$	c	18
$e + C_4F_8 \rightarrow C_3F_5^+ + CF_3 + e + e$	c	19
$e + C_4F_8 \rightarrow C_2F_4^+ + C_2F_4 + e + e$	c	19
$e + C_4F_8 \rightarrow F^+ + C_4F_7 + e + e$	c	19
$e + C_4F_8 \rightarrow CF_3^+ + C_3F_5 + e + e$	c	19
$e + C_4F_8 \rightarrow CF_2^+ + C_3F_6 + e + e$	c	19
$e + C_4F_8 \rightarrow CF^+ + C_3F_7 + e + e$	c	19

[a] Only reactions directly affecting species densities are included in the FKM. The additional electron impact collisions such as momentum transfer and excitation of vibrational and electronic states are included in the EETM to account for the transport and energy loses of the electron.

[b] Rate coefficients have units of cm^3/s unless noted otherwise.

[c] Rate coefficient is calculated from electron energy distribution obtained in the EETM using the cross section from the cited reference.

[d] Cross section was obtained by detailed balance.

[e] Estimated by analogy to NF.

[f] Estimated by analogy to CF_4.

[g] Estimated using Maxwellian distribution.

[h] Estimated by analogy to C_2F_6.

[i] Estimated by analogy to C_2F_4.

B.1 References

1 M. Hayashi, Nagoya Institute of Technology Report, No. IPPJ-AM-19, 1991.

2 K. Tachibana, Phys. Rev. A **34**, 1007 (1986).

3 D. Rapp and P. Englander-Golden, J. Chem. Phys. **43**, 1464 (1965).

4 R. H. McFarland and J. D. Kinney, Phys. Rev. **137**, 1058 (1965).

5 I. P. Zapesochnyi, Y. N. Semenyuk, A. I. Dashchenko, A. E. Imre and A. I. Zapesochyny, JETP Lett. **39**, 141 (1984).

6 L. Vriens, Phys. Lett. **8**, 260 (1964).

7 W. L. Morgan (private communication), Kinema Software, http://www.kinema.com

8 M. Hayashi and T. Nimura, J. Appl. Phys. **54**, 4879 (1983).

9 E. Meeks, J. Electrochem. Soc. **144**, 357 (1998).

[10] M. Tarnovsky and K. Becker, J. Chem. Phys. **98**, 7868 (1993)

[11] R. A. Bonham, Jpn. J. Appl. Phys., Part 1 **33**, 4157 (1994)

[12] V. Tarnovsky, P. Kurunczi, D. Rogozhnikov, and K. Becker, Int. J. Mass Spectrom. Ion Processes **128**, 181 (1993).

[13] M. Gryzinski, Phys. Rev. **138**, 336 (1965).

[14] K. Yoshido, S. Goto, H. Tagashira, C. Winstead, B. V. McKoy and W. L. Morgan, J. Appl. Phys. **91**, 2637 (2002).

[15] C. Winstead and B. V. McKoy, J. Chem. Phys. **116**, 1380 (2002).

[16] M. Hayashi and A. Niwa, in *Gaseous Dielectrics V*, edited by L. G. Christophorou and D. W. Bouldin (Pergamom, New York, 1987), pp. 27-33.

[17] V. Tarnovsky, H. Deutsch and K. Becker, J. Phys. B **32**, L573 (1999).

[18] G. I. Font, W. L. Morgan, and G. Mennenga, J. Appl. Phys. **91**, 3530 (2002).

[19] C. Q. Jiao, A. Garscadden, and P. D. Haaland, Chem. Phys. Lett. **297**, 121 (1998).

[20] A. V. Vasenkov, X. Li, G. S. Oehrlein and M. J. Kushner, J. Vac. Sci. Technol. A **22**, 511 (2004).